Journal of Research of the National Bureau of Standards

In This Issue:

Vol. 92, No. 5, September–October 1987

Departments

News Briefs and Reports

Conferences/Events

Articles

News Briefs and Reports

Developments

INITIAL STUDY OF ELECTRONIC STRUCTURE IN Y-Ba-Cu-O HIGH TEMPERATURE SUPERCONDUCTOR

Researchers in the NBS Surface Science Division have published one of the first papers on the electronics structure of the high-temperature superconducting ceramic $YBa_2Cu_3O_7$. Electronics structure, which describes the permissible energy levels of electrons in the material, is a critical piece of information for understanding the still-mysterious mechanism of high-temperature superconductivity. In experiments run in collaboration with colleagues from the Naval Research Laboratory, physicists Richard Kurtz and Roger Stockbauer used the NBS synchrotron light source and resonant photoemission to map the electronic structure above and below the transition temperature for superconductivity, and to identify the atoms which contribute to the important valence bands of the structure. The data show no major changes in electronic structure with the transition to superconductivity, and that the predominant copper valence state comes from Cu^{2+} atoms. Both results should significantly affect current efforts to develop a theory of high-temperature superconductivity. "Resonant Photoemission Study of Superconducting Y-Ba-Cu-O" appears in the Rapid Communications section of the June 1 issue of *Physical Review B.*

NBS RESEARCHERS SUCCESSFULLY OPERATE 10-VOLT JOSEPHSON ARRAY

Researchers at the NBS Boulder Laboratories have achieved an extremely precise 10-volt output from an array of superconducting Josephson junctions. The array may eventually serve as a new standard for the U.S. legal volt at an unprecedented level of accuracy for this voltage.

The scientists believe the new array has more active elements—over 14,000—than any previous fully operational superconducting integrated circuit. The main challenge in designing and fabricating this complex circuit lay in making such a large number of flawless junctions with sufficiently uniform properties. A 2-year program to improve NBS' microcircuit fabrication capability made the success possible.

Development of this array was driven by increasing demands for calibration of popular 10-volt Zener diode standards. Such standards are gradually replacing 1-volt Weston-type cells as secondary standards in industrial and military laboratories around the country.

The legal unit of voltage in the United States and most other countries is defined in terms of the ac Josephson effect, in which microwave radiation (very high frequency radio waves) impinging on a superconducting junction generates quantized voltage steps that are exactly proportional to the frequency and to the ratio of Planck's constant to the electron charge. Since the latter ratio has been internationally defined, it is possible in principle to measure voltage as accurately as frequency, which is to say, as accurately as any physical measurement can be made at present.

Each Josephson junction can generate only a few millivolts. Previous 1- or 2-junction Josephson standards required the use of a complicated resistance bridge to compare the tiny standard voltage with that of devices being calibrated. Increased accuracy is possible when many Josephson junctions in series can be fabricated on a single chip, eliminating the need for the resistance bridge.

During the late 1970s, the Bureau contributed to research on Josephson junctions which revealed a possible method for connecting many junctions in series to provide high output voltages. NBS' Richard Kautz first demonstrated the new mode of operation for Josephson standards in 1980. By

March 1987, an array of 2076 junctions operating at the 1-volt level was placed in service as the new official U.S. legal volt standard. A month later, researchers Frances Lloyd, Clark Hamilton, James Beall, Diane Go, Ronald Ono, and Richard Harris succeeded in operating an array of 14,184 Josephson junctions to provide a 10-volt output, realizing a voltage standard at an even more useful level.

These long arrays of superconducting junctions are constructed using technology borrowed from the semiconductor integrated circuit industry, substituting thin films of superconducting metals such as lead and niobium for the semiconductors. Various patterned layers of superconductors and insulators are deposited onto insulating thumbnail-sized substrates. They must then be cooled to within 4 degrees of absolute zero to reach the superconducting state.

The potential accuracy of the voltage determined using these arrays is essentially the same as the accuracy of the frequency used to irradiate the junctions. Atomic clocks could be used as a source of the frequency to provide an accuracy of better than 1×10^{-13}. However, for useful calibrations, noise and other practical limitations at present limit voltage accuracy to a few parts in 100 million.

GENCORP, INC. TO STUDY ELASTOMER BLENDS AT NBS

A joint research program to develop quality control information for the manufacture of tires and advanced elastomer products made from polymer blends has been established between NBS and GenCorp, Inc. Leon F. Marker and John J. Beres of the Akron, Ohio-based GenCorp are synthesizing samples of butadiene polymers, copolymers, and other elastomeric blends for examination of their microstructures by small-angle neutron scattering (SANS) at the NBS research reactor. The SANS technique allows these scientists to determine the phase separation of molecules as a function of temperature and composition. SANS measurements will be used by the researchers to develop phase diagrams showing the mixing and curing times required to obtain specific properties in polymer materials.

The joint project is part of the NBS Research Associate Program, which provides an opportunity for people from industry, universities, technical societies, and other organizations to conduct cooperative research at the Bureau on programs of mutual interest. Salaries are paid by the sponsor.

For further information on RAP, contact David Edgerly, Rm. A402 Administration Building, National Bureau of Standards, Gaithersburg, MD 20899, or call 301/975-3087.

NEW TECHNOLOGIES, QUALITY IMPROVEMENT, GLOBAL COMPETITION PUSH DEMAND FOR BETTER MEASUREMENTS

New technologies, the push for improved product quality, and global competition are dramatically increasing the demand for new measurement-related research and services, according to a report NBS delivered to Congress in late June [1].

The report was prepared at the request of the House Committee on Science and Technology and the Senate Committee on Commerce, Science and Transportation. It reviews current NBS measurement-related services to industry, government, and academia, and includes the views of key organizations which rely on those services. As part of the study, NBS officials visited senior managers in industry and government.

Among the study's conclusions:

– Industry needs greater numbers of individual measurements over a diversity of parameters and ranges. Because very high-accuracy measurement capability is being built into commercial devices, NBS needs to develop more measurement standards which are based on the invariant properties of matter which can be used in such devices (e.g., electrical/electronic measurement and test structures on a picosecond time scale.)

– Mature technologies need calibration services such as mass, flow, force, temperature, pressure, and optical radiation to be maintained, refined, or advanced.

– The trend toward real-time feedback and modification of process control and quality assurance systems will require different and better sensors, measurement devices, and calibration methods.

– Industrial concern for quality seems to be translating into concern for achieving traceability to NBS, which is increasing demand for NBS Standard Reference Materials (SRMs) of all types. In particular, new emerging technologies have produced a growing demand.

– "Multi-parameter" SRMs in which both physical and chemical properties are certified for the same materials are of especially high priority for the future.

– U.S. industry has come to rely on the Bureau's SRMs to calibrate "relative" measuring instruments (automated devices which do not measure absolutely). Most firms no longer have any laboratory capability of their own to calibrate such instruments.

The report includes a summary of specific measurement needs in advanced materials, advanced

electronics and semiconductors, microwave systems, automation, biotechnology, computer applications, electro-optics, physics and chemistry, and safety and health.

Reference

[1] Process and Quality Control and Calibration Programs of the National Bureau of Standards, available by sending a self-addressed mailing label to: Program Office, A1002 Administration Building, National Bureau of Standards, Gaithersburg, MD 20899.

NBS CONSORTIUM ORGANIZED TO HELP METAL POWDERS INDUSTRY

ALCOA, Crucible Materials Corporation, General Electric Company, and Hoaganaes Corporation are the first private sector organizations to join a new consortium established by NBS. The consortium's goal is to develop the basic measurement system needed for the automated or "intelligent" processing of rapidly solidified metal powders by high-pressure, inert-gas atomization. The 3-year program is open to researchers from industry, universities, and government agencies who are concerned about quality control in the production of rapidly solidified metal powders for aerospace and other high-technology products that require materials with superior performance. These powders can be processed into usable parts to near-net shape by various consolidation methods such as extrusion and hot pressing that generally preserve the rapidly solidified microstructures.

For information on the consortium, or to join the program by providing either funds or researchers, contact Tom Yolken, B344 Materials Building, National Bureau of Standards, Gaithersburg, MD 20899, or call 301/975-5727.

GUENSLER BECOMES CHAIRMAN OF NCWM AT 72ND MEETING

Darrell A. Guensler, who heads the Division of Measurement Standards in the California Department of Food and Agriculture, has been chosen chairman of the National Conference on Weights and Measures (NCWM). Guensler, active in weights and measures activities for 25 years, assumed office at the July 1987 NCWM annual meeting in Little Rock, AR.

NCWM is an organization of state, county, and city weights and measures enforcement officials and associated business and consumer representatives. Through the NBS Office of Weights and Measures, the Bureau provides technical assistance to NCWM and its committees.

For information on the conference, contact the National Conference on Weights and Measures, P.O. Box 3137, Gaithersburg, MD 20899, or call 301/975-4004.

SYNTHETIC HYBRID LUBRICANTS STUDIED AT NBS

Working jointly with NBS scientists, researchers from Technology Assessment and Transfer, Inc., Gambrills, MD, have shown that it is possible to develop a hybrid solid-liquid lubricant with improved performance for use in high-temperature friction and wear environments. Using NBS' high-temperature sliding wear test system, the researchers conducted studies on various combinations of synthetic lubricants with liquid and dry powder additives. The formulations consisted of nickel and chromium intercalated graphites at concentrations of about one-weight percent in the liquid carriers. Tests were performed up to 500 °F under highly loaded boundary lubrication conditions.

Further studies also indicated that solid composites of metal or ceramics with these intercalated graphites may have desirable wear and friction characteristics for such applications as ring-liner combinations in high-temperature engines. The work is being done as part of the NBS Research Associate Program, which provides an opportunity for people from industry and other organizations to conduct cooperative research at the Bureau on programs of mutual interest. Salaries are paid by the sponsor.

For further information on RAP, contact David Edgerly, Rm. A402 Administration Building, National Bureau of Standards, Gaithersburg, MD 20899, or call 301/975-3087.

ANTENNA MEASUREMENT ERRORS DESCRIBED, EVALUATED

When antennas are measured or calibrated in anechoic chambers, a misalignment of the receiving and source antennas will lead to errors. In the case of near-field measurements, uncertainty about the location of the probe with respect to the antenna will cause relatively large errors. Two recently published reports from NBS rigorously examine these errors to quantify their effects on measurement accuracy. *Evaluation of Off-Axis Measurements Performed in an Anechoic Chamber* (TN 1305) and *Displacement Errors in Antenna Near-Field Measurements and Their Effect on the Far Field* (TN 1306) are available from the Superintendent of Documents, U.S. Government Printing Office, Washington, DC 20402. TN 1305 may be ordered for $2.25 prepaid; order by stock no. 003-003-02779-1. TN 1306 costs $2 prepaid; order by stock no. 003-003-02776-6.

CHEMICAL REACTIONS LEADING TO SOOT FORMATION REVIEWED

For several years, NBS chemists Kermit C. Smyth and J. Houston Miller have been studying the chemical reactions in flames that lead to soot formation. In an article in *Science* magazine [1], Smyth and Miller review their studies and discuss their most recent research. The NBS scientists say that identifying the detailed mechanisms by which large hydrocarbon molecules are produced during combustion continues to be one of the most challenging problems in high-temperature chemistry. But through recent laboratory experiments and computer modeling at NBS and other organizations, significant progress has been achieved in identifying the growth reactions that lead to soot inception. Smyth and Miller speculate that a single, dominant mechanism may be involved in soot formation for all types of flames. Understanding this process is important for several reasons. Soot is a particular problem during a fire because it hinders vision and impairs breathing, and soot formation plays a key role in efficient burning and energy transfer such as in power plants.

Reference

[1] Smyth, K.C.; J.H. Miller, Chemistry of Molecular Growth Processes in Flames, Science, Vol. 236, No. 4808: 1540-1546; June 19, 1987.

NBS Services

NBS RECOMMENDS 400TH ENERGY-RELATED INVENTION FOR ASSISTANCE

A new process for continuous casting of steel cylinders used in manufacturing seamless pipe and tubing recently became the 400th invention to be recommended by NBS to the Department of Energy (DoE) for possible assistance in development and marketing.

Through the Energy-Related Inventions Program, conducted jointly by NBS and DoE, inventors can receive help in getting their ideas from the workshop to the marketplace. NBS provides, at no cost to the inventor, evaluations of energy-related inventions and recommends those it considers promising to DoE. In turn, DoE can provide financial support or help in marketing an inventor's idea.

The 400th invention to get NBS' recommendation is the idea of Gerhard E. Schwarz of Avon Lake, OH. Schwarz, a former senior engineer at the USX Corporation, has developed a way to continuously cast hollow, round steel cylinders used to manufacture seamless steel pipe and tubing.

About a million tons of seamless steel pipe and tubing worth roughly a billion dollars is used annually by the gas, oil, and power-generating industries as well as by chemical processors. Seamless pipe and tubing are in demand because it is strong, more reliable, and allows the use of thinner walls—and, thus, less material.

Continuous casting substantially reduces production costs, raises yields and productivity, and improves product quality. But the use of this technology in the United States is well below the levels of other major industrialized countries. During the first half of 1986, 49 percent of all raw steel processed in the United States was continuously cast; in 1985, 91 percent of the raw steel processed in Japan was continuously cast, and 71 percent in the European community.

The conventional method for manufacturing seamless steel pipe starts with solid ingots which first must be shaped into billets—short, thick bars of steel. They are then reheated, hollowed out, stretched, reheated, and finished. Schwarz's method, for which he holds a patent, would eliminate many of these steps by initially pouring the molten steel into a cooled vertical mold which forms a hollow round. Other attempts have been made, both in the United States and abroad, to cast hollow rounds, but so far these methods have not produced high-quality steel.

George Lewett, chief of the NBS Office of Energy-Related Inventions, says Schwarz's invention could save the equivalent of 200,000 or more barrels of oil per year. But, adds Lewett, "the principal value of Schwarz's process is expected to be a higher quality product which should cost no less to produce. This would give American manufacturers of seamless pipe and tubing a significant competitive advantage in an area that has been heavily invaded by imports." According to the Bureau of the Census, in 1985 the United States imported more than 4 million tons of all types of steel pipe and tubing, including seamless, worth about $2.4 billion.

Inventors getting a favorable NBS review are a relatively select group, those with very promising, new ideas. Of the 23,700 inventions submitted to NBS since the program started in 1975, NBS has recommended just 400 for DoE assistance.

These inventions have ranged from a portable pothole patcher, to a new way of making a composite material, to a new packing ring that could save electric utilities up to $200 million annually.

Many of the inventions have been successfully introduced into the market. According to a recent evaluation of the program conducted by

Oak Ridge National Laboratory, 70 of 204 recommended inventions that were studies were commercialized by 1985. They accounted for more than $200 million in sales from 1976 through 1984.

For example, California inventor Norman Fawley designed a lightweight aluminum cylinder, reinforced with resin-impregnated glass filaments, which makes it practical to use natural gas as a vehicle fuel. The cylinders being produced by Fawley's company, now a subsidiary of Aluminum Company of America (ALCOA), have been installed in fleet vehicles of 20 companies in the United States and Canada. John A. McDougal of Detroit, MI, developed a system that senses knocking in an automobile engine and controls spark timing in individual cylinders. McDougal recently licensed his system to the Ford Motor Co. in exchange for royalties.

An invention that passes initial NBS review undergoes a rigorous evaluation by the staff of the NBS Office of Energy-Related Inventions, relying in part of a national network of hundreds of expert consultants from government, industry, and universities. Typically, NBS evaluators obtain written opinions from at least two consultants on each invention evaluated.

The engineer-evaluators ask three key questions: Is the invention technically feasible? Will it save a significant amount of energy or increase supplies from nonnuclear sources? Does it have a reasonable chance of becoming a commercial success?

If the invention is considered promising, NBS forwards it to DoE for financial support and/or help with marketing the invention. The one-time DoE grants typically have ranged between $50,000 and $200,000, with an average of $80,000 per invention.

Inventions that are not recommended to DoE do get the benefit of a free evaluation by NBS. If an invention does not warrant further review, the key reasons are identified and sent to the inventor, who is welcome to try again. "We're always willing to reconsider our position if the inventor can provide further details or new information," says Lewett.

The assistance the program gives to inventors does not stop at evaluations and financial and marketing support. For the past 7 years the program has been bringing together inventors through a series of National Innovation Workshops held nationwide. The 2-day workshops give practical guidance and information to inventors and prospective inventors through lectures and panel discussions. Advice is given on turning ideas into inventions, and getting help from both public and private sources. More than 5000 inventors and would-be inventors have attended these workshops.

Those with ideas that will help save energy or who would like information on the workshops should write to:

Office of Energy-Related Inventions
Room 209 Engineering Mechanics Building
National Bureau of Standards
Gaithersburg, MD 20899

USERS, VENDORS COMPLETE OSINET FILE TRANSFER TESTS

The first group of 13 computer users and vendors has completed a series of tests across OSINET, an experimental computer network for Open System Interconnection (OSI) standards. The group succeeded in accessing, transferring, and managing files as well as demonstrating that their OSI systems could work together. Coordinated by NBS, this network is helping to speed the development and use of commercial OSI products in industry and government.

Twenty-two computer and communications manufacturers and users, including several government agencies, are participating in the program. OSINET participants have developed their implementations of OSI standards, called "protocols." Using these implementations to communicate with each other and with the Network Information Center located at the NBS, product developers are able to verify that their systems work with other systems.

The file transfer protocol implementations in use by the OSINET participants are based on agreements reached at the NBS ongoing workshops for implementors of OSI. More than 200 computer manufacturers, semiconductor manufacturers, word processing vendors, process control vendors, communications carriers, and industry and government users participate in the workshops to advance the development of commercial products implementing OSI standards. The OSINET Steering Committee recently invited nonparticipants to submit proposals for joining the network.

For more information, contact Gerard Mulvenna, B217 Technology Building, National Bureau of Standards, Gaithersburg, MD 20899, or call 301/975-3631.

Journal of Research of the National Bureau of Standards

An Automated Potentiometric System For Precision Measurement Of the Quantized Hall Resistance

Volume 92 Number 5 September-October 1987

Giancarlo Marullo Reedtz

Istituto Elettrotecnico Nazionale
Galileo Ferraris,
Strada delle Cacce 91
10135 Torino, Italy

Marvin E. Cage

National Bureau of Standards
Gaithersburg, MD 20899

This paper describes the development of an automated potentiometric measurement system that is used to compare the quantized Hall resistance with that of wire-wound reference resistors having the same nominal value. Conceptual considerations, along with the major practical problems associated with this method, are presented. We then report experimental results which demonstrate that this measurement system is accurate to within a 0.007 ppm one standard deviation uncertainty.

Key words: electrical metrology; ohm; precision measurements; quantized Hall resistance; quantum Hall effect; resistance standards.

Accepted: March 27, 1987

1. Introduction

The quantization of the Hall resistance

$$R_H(i)=\frac{h}{e^2 i}\approx\frac{25{,}812.80}{i}\Omega, \quad (1)$$

(where h is the Planck constant, e the electron charge, and i an integer quantum number) has been demonstrated for such diverse two-dimensional electron systems as those in Si-MOSFETs [1][1] or in heterostructure devices (GaAs/AlGaAs [2] and more recently InGaAs/InP [3]). This resistance quantization provides a very promising means to yield not only a constant and reproducible as-maintained unit of resistance but to determine also, by solid state physics techniques, the fine structure constant α [4,5]. Even if the physical phenomenon (as manifested in real samples) is not completely understood, the experimental results from different national laboratories show an agreement between R_H values of a few parts in 10^7 [6] when using different samples and measurement systems.

The precision measurement of R_H requires three main steps: 1. the metrological characterization of the sample so that a reasonable confidence is reached on the independence of the measured value from the experimental conditions—mainly temperature and current through the sample [7,8]; 2. the comparison of R_H with the resistance R_R of a highly stable reference resistor; and 3. the calibration of R_R in terms of either the as-maintained unit of resistance or in terms of the International System (SI) resistance unit.

About the Authors: Giancarlo Marullo Reedtz is a physicist at the Galileo Ferraris National Electrotechnical Institute, and Marvin E. Cage, who is with the Electricity Division in the NBS Center for Basic Standards, is also a physicist.

[1]Figures in brackets indicate literature references.

An automated potentiometric system has been built to compare, as in step 2, the value of R_H with a nominally equal reference resistance R_R within a one standard deviation (1σ) uncertainty of 0.007 ppm (parts per million). This system, which replaces and improves an earlier manually-operated version, is flexible enough to be used also for the precision measurements required in step 1.

2. Comparison of R_H and R_R

The conceptual scheme of the measurement circuit is shown in figure 1, where the numerical values are specific to the case when $R_H = 6{,}453.20\ \Omega$ (the $i=4$ Hall plateau) and the current is $I = 25\ \mu A$. The two resistances to be compared are connected in series, and the high impedance nanovoltmeter D measures the differences between each voltage drop V_H or V_R and the compensation voltage V_C. The switch S_1 enables the current direction and the compensation voltage both to be reversed so that the influence of thermal-electric voltages can be reduced; S_2 allows for switching between V_H and V_R. Therefore, S_1 must not change the resistance of the current circuits too much for the two polarities, and S_2 must introduce only a minimum amount of thermal voltages in the voltage circuit.

The measurement sequence needed for a single determination of the ratio R_H/R_R should be chosen to reduce the influence of the thermal voltages and the voltage and current drifts, while also trying to minimize the number of switching operations. Using the letters H or R to represent the comparisons between V_H or V_R and V_C (switch S_2), and the symbols + and − for the two current polarities (switch S_1), we consider the following sequence of operations:

$$R^+, R^-, H^-, H^+, H^+, H^-, R^-, R^+. \qquad (2)$$

Within each pair of +/− measurements, the influence of the thermals, if constant, is eliminated by the current reversal. The circuit in figure 1 is also affected by changes in the thermals, and by drifts in the voltage generators E and E', or in the currents. Linear drifts in the circuit can be represented as changing currents by the relations

$$I(t) = I(0)(1+\beta t)$$
$$I'(t) = I'(0)(1+\beta' t). \qquad (3)$$

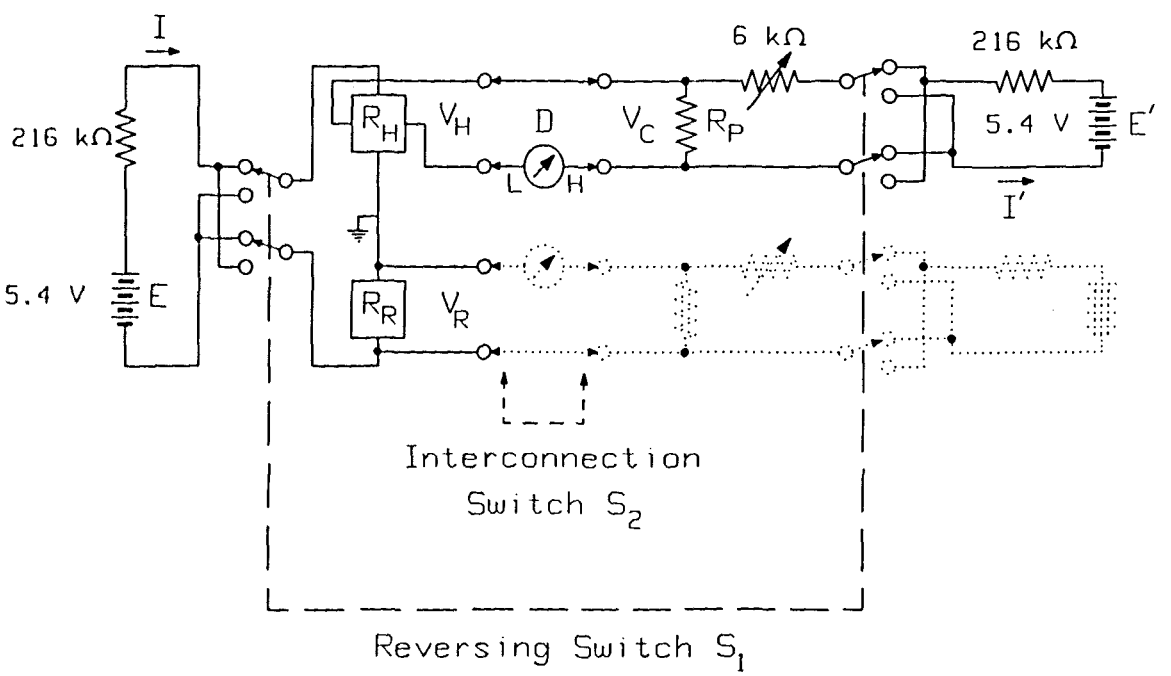

Figure 1-Schematic diagram of the automated potentiometric measurement system which compares the quantized Hall resistance R_H with a nominally equal reference resistor. The voltage sources E and E' are thermally insulated mercury batteries. D is a Leeds & Northrup 9829 Linear Amplifier.

Neglecting constant thermals, we consider a sequence of four measurements R, H, H, R where the following relationships hold:

$$\begin{aligned} I(t_1)\cdot R_R &= I'(t_1)\cdot R_P - D(t_1) \\ I(t_2)\cdot R_H &= I'(t_2)\cdot R_P + D(t_2) \\ I(t_3)\cdot R_H &= I'(t_3)\cdot R_P + D(t_3) \\ I(t_4)\cdot R_R &= I'(t_4)\cdot R_P - D(t_4) \end{aligned} \tag{4}$$

where $D(t)$ is the reading of the detector at time t, and R_P is the potentiometer resistance as labeled in figure 1. If the measurements are uniformly spaced with time intervals Δt, then using eqs (3) and (4) and dividing the sum of the R_H equations by the sum of the R_R equations, we obtain

$$\frac{R_H}{R_R} = \frac{1+\dfrac{D(t_2)+D(t_3)}{2V_C(\bar{t})}}{1-\dfrac{D(t_1)+D(t_4)}{2V_C(\bar{t})}}, \tag{5}$$

where

$$V_C(\bar{t}) \equiv R_P\cdot I'(0)(1+\beta'\bar{t}) \tag{6}$$

and $\bar{t}=t_1+\frac{3}{2}\Delta t$ is the mean time of the four measurements.

If the two resistance values are different by a small amount we can expand the denominator in eq (5); neglecting second-order terms:

$$\frac{R_H}{R_R} \cong 1+\frac{1}{V_C}\left[\frac{D(t_1)+D(t_4)}{2}+\frac{D(t_2)+D(t_3)}{2}\right]. \tag{7}$$

Here the compensation voltage V_C has been written as time independent, which it is in the limits that we require (e.g., V_C need only be constant to 1 part in 10^3 for D/V_C ratios of 10^{-5} if we want an accuracy of 1 part in 10^8). Within these limits the drift of V_C has no influence in eq (7).

We now examine what happens if the switch S_1 introduces slightly different resistances for the two polarities of the I and I' circuits. Let the currents for the two polarities be I and $(-I'+\Delta I')$ for the circuit E, and in a similar way I' and $(-I'+\Delta I')$ for the voltage compensation circuit E'. Consider two successive pairs of measurements R^+, R^- and H^-, H^+. We can write the relations for the respective detector voltages:

$$\begin{aligned} D_R^+ &= I'\cdot R_P - I\cdot R_R \\ D_R^- &= (-I'+\Delta I')\cdot R_P - (-I+\Delta I)\cdot R_R \\ D_H^- &= -(-I'+\Delta I')\cdot R_P + (-I+\Delta I)\cdot R_H \\ D_H^+ &= -I'\cdot R_P + I\cdot R_H. \end{aligned} \tag{8}$$

Subtracting and dividing each pair by two:

$$\begin{aligned} D_R^* &= \frac{D_R^+ - D_R^-}{2} = I'\cdot R_P - I\cdot R_R - \frac{\Delta I'\cdot R_P}{2} + \frac{\Delta I\cdot R_R}{2} \\ D_H^* &= \frac{D_H^+ - D_H^-}{2} = -I'\cdot R_P + I\cdot R_H + \frac{\Delta I'\cdot R_P}{2} - \frac{\Delta I\cdot R_H}{2}. \end{aligned} \tag{9}$$

Adding and reordering:

$$\frac{R_H}{R_R} = 1+\frac{D_R^*+D_H^*}{I\cdot R_R} - \frac{\Delta I}{2I}\left[1-\frac{R_H}{R_R}\right]. \tag{10}$$

The last (third) term in eq (10) gives a second-order correction if the two resistances to be compared are nearly equal and the variation $\Delta I/I$ is small enough. As before, the denominator of the second term need only be known with limited accuracy and can be replaced by the compensation voltage V_C.

As a conclusion of this analysis we note that: a) the sequence given by eq (2) eliminates the effects of constant thermals within each pair of current reversal measurements; b) the symmetrical sequence eliminates the effects of linear drifts of thermals and of I and I'; and c) the measurements are not influenced by the slightly different values of I and I' for the two current polarities because each polarity is used to compare both V_H and V_R with the same compensation voltage V_C.

The measurement sequence actually used is a little more complex but fulfills all the requirements outlined above. It can be represented by

$$\begin{aligned} &R^+,R^-,R^-,R^+,\ H^+,H^-,H^-,H^+, \\ &H^+,H^-,H^-,H^+,\ R^+,R^-,R^-,R^+. \end{aligned} \tag{11}$$

This sequence provides a single value of the ratio R_H/R_R. If we call the mean values for each group of four measurements D_1, D_2, D_3, and D_4, and if we define

$$\begin{aligned} D_R &= \frac{D_1+D_4}{2} \\ D_H &= \frac{D_2+D_3}{2} \end{aligned} \tag{12}$$

then the relationship for the R_H/R_R value is

$$\frac{R_H}{R_R}=1+\frac{D_H}{V_C}+\frac{D_R}{V_C}. \quad (13)$$

3. Sample Characterization and System Flexibility

Every prospective sample must be characterized to establish what experimental conditions are required in order to ensure that the measured values of R_H have the desired accuracy [7,8]. The following measurements of R_H and of R_X (the sample resistance in the direction of the current) are made before a device is considered for precision R_H/R_R comparisons: 1) R_H and R_X as a function of the sample temperature; 2) R_H and R_X as a function of the current through the sample; 3) as in items 1) and 2), but for different pairs of R_H and R_X contacts and for both magnetic field directions; and 4) R_H values for different points along the Hall plateau to verify its flatness.

All these measurements require precision comparisons between R_H and R_R. For item 2) the compensation voltage for R_H measurements must be varied over a wide range. Also, a high impedance current source is required to maintain constant current when the sample is not in a well-quantized regime. The potentiometric comparison circuit of figure 1 has been built in modular form to allow for these different measurement conditions. A functional diagram of the components of this circuit is shown in figure 2, where solid (dashed) lines are for current (voltage) connections. Dashed lines also symbolize output signals that are measured or recorded.

The Potentiometer Box in figure 2 provides the functions needed for the highest precision measurements. The currents I and I' are generated using matched sets of thermally insulted mercury batteries and fixed-value resistors. Comparisons of R_H/R_R can be made at 10 μA and 25 μA for $i=4$ Hall steps and at 25 μA for $i=2$ steps. These currents are small enough to provide accuracies better than 1 part in 10^8 for the three GaAs samples so far characterized.

An electronic, high impedance, constant current source can replace the mercury battery source I of the Potentiometer Box for current dependence measurements and for measurements off of the step. The electrical noise, however, is an order of magnitude higher with the constant current source. A high stability solid-state Zener voltage source followed by a Kelvin-Varley resistance divider can substitute for the battery current source and fixed divider. These again are an order of magnitude noisier.

The Sample Patch Box allows for easy connection of the current leads to the source and drain, as well as to any pair of potential pads on the sample, e.g., V_H or V_X. The voltages read by the detector can either be direct or compensated by V_C.

Each Reference Resistor Box contains an Electro Scientific Industries resistor[2], composed of series/parallel combinations of wire-wound resistors constructed to have R_R values within a few ppm of the value of R_H. They are hermetically sealed in a silicone fluid-filled container and placed in a specially constructed temperature-regulated air bath enclosure. The air temperature is controlled to within ± 0.002 °C at a nominal temperature of ~ 28 °C.

The Calibration Box contains an adjustable voltage source whose polarity can be reversed by the Hewlett Packard 9836 computer. This box, when connected to the detector input, enables the detector-digital voltmeter combination to be calibrated.

Finally, R_H and R_R can be easily interchanged in the measurement circuit to check for systematic errors. We have found this test to be essential.

4. Construction Considerations

4.1 The Insulation Resistance

The high values of the resistances to be compared (6,453.20 Ω or 12,906.40 Ω for $i=4$ or $i=2$ steps, respectively) require an insulation resistance of the circuit of about 10^{12} Ω to achieve an uncertainty of the order of 10^{-8}. As a rule, polytetrafluoroethylene (PTFE or Teflon) has been used as the insulating material. Great care was taken in cleaning the insulating parts of cables and connectors with alcohol. This provides leakage resistances greater than 10^{14} Ω.

The switching is done by Leeds & Northrup 4 pole, 12 position, rotary switches with Lexan wafers (model number 031264). The leakage resistance is 5×10^{13} Ω for each connection. Multiple connections reduce this value. The nanovoltmeter detector D is a Leeds & Northrup 9829 Linear Amplifier. Its input low is only isolated by 10^{10} Ω from

[2]Brand names are used only for purposes of identification. Such use implies neither endorsement by the National Bureau of Standards nor assurance that the equipment is the best available.

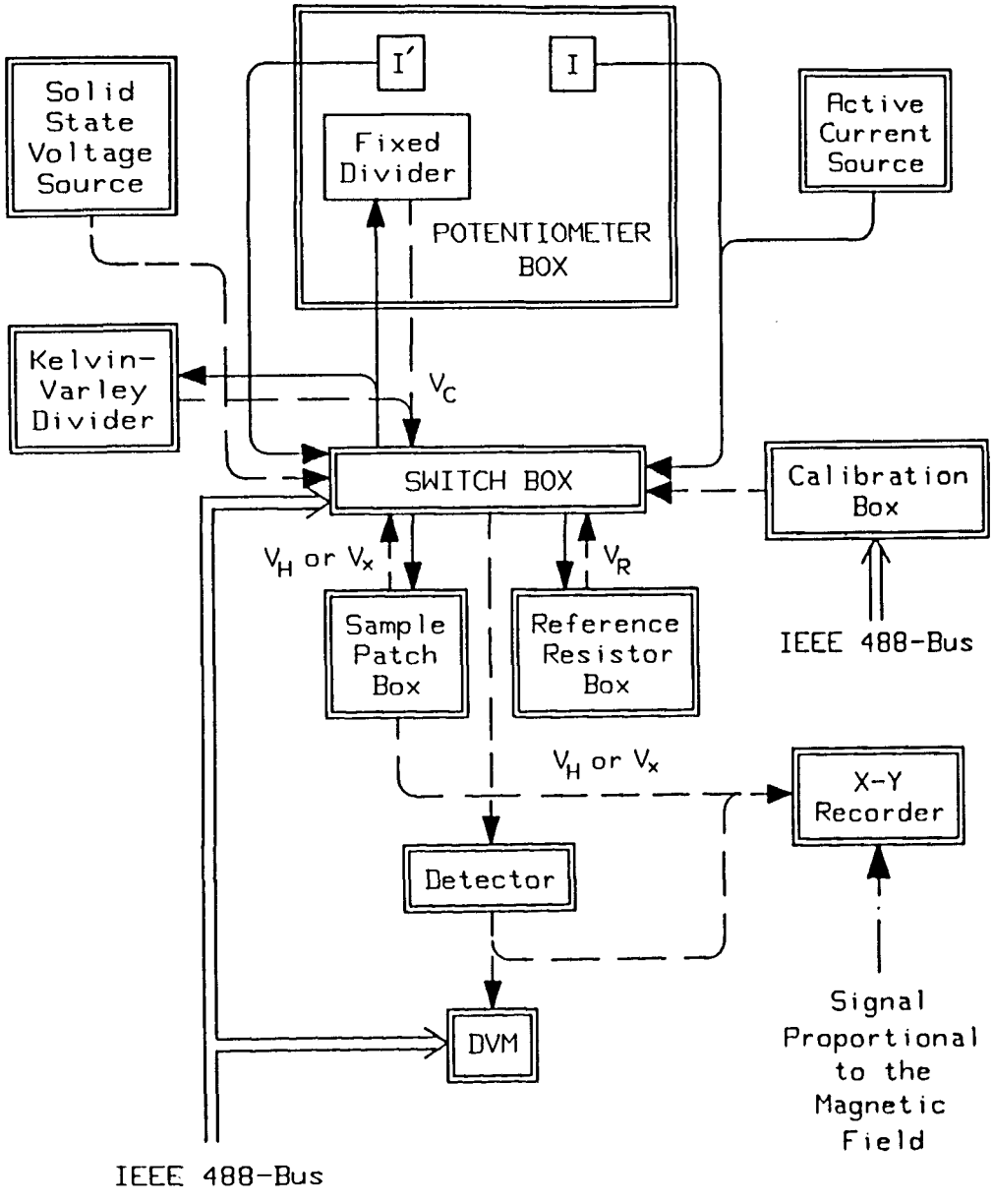

Figure 2–Functional block diagram of the measurement system. This figure stresses the interchangeability of different components to enable the highest precision measurements as well as the physical characterization of the Hall sample. Solid lines represent the current-related functions and dashed lines the voltage-related functions. (There are, of course, actually two paths for every line drawn in the figure.) See the text for further explanation.

the nanovoltmeter guard circuit. Therefore, the detector input low is always connected to the potential point nearest circuit ground, and the guard is also connected to this ground. (The low potential point, of course, changes sides on the sample if the magnetic field direction is reversed.)

The complete potentiometric measurement system has an insulation resistance of 3×10^{12} Ω when the humidity is less than 50%. This leakage resistance is periodically monitored to ensure that dust, lint, hair, and fingerprints have not reduced it.

4.2 Contact Resistances, Thermal-Electric Voltages, and Drifts

The cables consist of sets of twisted pairs of PTFE-insulated, silvered, stranded copper wires enclosed within two separate coaxial shields.

British Post Office connectors (model numbers OFF 66148 and 66149) are used whenever possible because they have small and reproducible contact resistances, high leakage resistances, and are completely shielded.

Fixed connections are made by a low melting point Sn-Pb alloy solder, rather than a low thermoelectric power Sn-Cd alloy, because of better mechanical strength and more reliable electrical contacts. Tightly-packed thermal insulation is used to minimize temperature gradients.

The contact resistances of the Leeds & Northrup rotary switches are less than 0.7 mΩ and have a reproducibility of 0.05 mΩ. Differences in resistance of the two current circuits, due to slightly different lengths of the wires through the switches for each polarity, are less than 4 mΩ. That value is less than 2×10^{-8} of the resistance of each circuit. As shown in section 2, this has no detectable influence on the result when using the sequence of measurements shown in expression (11). These switches exhibit less than 20 nV thermals 10 seconds after repeated switching.

The drifts of the I and I' sources are of the order of 0.2 ppm or less during the 12 minute time intervals required to carry out the measurement sequence of expression (11). This small drift rate is achieved by using careful thermal insulation of the Potentiometer Box, and by not opening the loads during current reversals. (Momentary double loads in the make-before-break switching are better than open-circuiting for the stability of the mercury batteries.)

4.3 The Automated Switching

Stepping motors have been used to rotate the switches S_1 and S_2. They are Clifton Precision model 23-SHAB-49BU motors with a minimum rotation of 0.9°/step and a 0.45 N·m torque. The motors must overcome a significant frictional force. As a result, they occasionally can miss steps. After several misses the switches may open-circuit. To prevent this we realign the switches by deliberately forcing the motors to rotate the switches against stops.

The motors are controlled by a driver (a Clifton Precision model DPB05) which supplies the clock pulses that control the steps, and other TTL signals which determine the direction of rotation, the working mode (0.9°/step or 1.8°/step), and the current-off-after-switching capability. The last feature is useful to reduce the noise in the system during measurements and to allow for manual switch operation.

4.4 Noise Problems

Great care has been used in shielding the system. Two independent levels of electrostatic shielding have been provided for all the boxes and cables within the instrument. In addition, the electronics rack for the instrument, aluminum shelves for the reference resistors, metal room walls, and copper pipe for the signal cable to the cryostat give a third, nearly complete, shielding level that is electrically insulated from the other two shields. The only exceptions are: the reference resistor boxes which have only two levels of shielding, and the cryostat and quantum Hall sample holder with just one independent shield.

To avoid current loops, all cables have their coaxial shields broken on one side. Shielding connections among different chassis boxes are made by dedicated cables. Only one connection exists between different shielding levels, between the instrument rack and laboratory ground, and between the first shield and the measurement circuit. This last connection can be opened for the leakage resistance tests.

The largest amount of electrical noise in the system comes from the nanovoltmeter detector, which has 150 nV peak-to-peak noise within a 0.5 Hz bandwidth. This noise (obtained with the input short-circuited and with the instrument powered by batteries) corresponds to about 38 nV at the 1σ level, to be compared with 7 nV (1σ) Johnson noise of a 6,453.20 Ω resistor at room temperature within the same bandwidth.

The nanovolt amplifier noise is about 25×10^{-8} of the voltage to be compared for a current of 25 μA on the $i=4$ step. Therefore, long integration times must be used on the detector output to obtain uncertainties less than 1×10^{-8} for the standard deviation of the mean of a R_H/R_R comparison.

For each operation of the sequence given in expression (11), the computer takes 60 readings in 30 s time intervals from a digital voltmeter at the output of the detector. A wait time of 15 s is introduced after switching. It takes 12 minutes to complete one sequence and thus yield a single value of the ratio R_H/R_R. The standard deviation[3] of such a sequence is typically 0.016 ppm. The value is the same whether the reference resistor is compared with a quantum Hall resistor or with another reference resistor. Seven sequences (84 minutes of measurements) are usually sufficient to obtain a standard deviation of the mean (random uncertainty) of 0.006 ppm.

[3]Throughout, all uncertainties are meant to correspond to one standard deviation estimates.

5. System Performance

This measurement system has been in operation since August, 1986 to compare the value of R_H for the $i=4$ plateau of a GaAs/AlGaAs heterostructure with that of two nominally equal 6,453.20 Ω reference resistors, and to also intercompare the two reference resistors. Table 1 summarizes the estimated uncertainties assigned to quantum Hall sample-reference resistor intercomparisons for a 25 μA current.

Table 1. Estimated one standard deviation (68% confidence level) uncertainties for the quantum Hall resistance measurements at 25 μA.

$R_H \leftrightarrow R_R$

Sources of Uncertainty	Uncertainty (ppm)
Random	0.004
Sample-Resistor Interchange	0.004
Detector Gain Stability	0.003
Leakage Resistance	0.002
QHR Temperature Dependence	0.002
QHR Current Dependence	0.001
ROOT-SUM-SQUARE TOTAL (ppm)	0.007

The standard deviation of the mean (the random or type A measurement uncertainty) is, as noted above, typically ±0.006 ppm for a sample-resistor comparison. The position of the sample and resistor are then interchanged in the measurement system and the values are remeasured. The Hall resistance value assigned is the unweighted mean of these two comparisons, and the random uncertainty of the 14 pooled measurements is usually ±0.004 ppm. Pooling all of the measurements is viewed as justified since usually the difference in the values obtained in the two positions is well within the scatter of the data.

In addition to the random uncertainties, there are systematic, or type B, uncertainties associated with systematic corrections and other effects. One such correction is due to a measurement system offset, or interchange, error in which the value of the Hall resistance depends on whether it is measured in the R_H position or in the R_R position of the measurement circuit. The largest interchange correction to date has been +0.013 ppm, but, as noted above, is usually much less (i.e., indiscernible; the correction is based on the assumption that the mean of the two values obtained is the correct value). It is not completely understood why the interchange correction is less of a problem in this measurement system than it is in the old version of the potentiometric system [9] and in the automated bridge system [9,10]. Perhaps it is due to a higher leakage resistance and to better electrical shielding. The estimated type B uncertainty associated with the interchange correction is assumed to be the same as the random uncertainty: ±0.004 ppm.

There is an uncertainty in calibrating the gain of the electronic detector-digital voltmeter pair. The pair can *appear* to vary by a few tenths of a percent over the input voltage range if the DVM has a dead-band at zero volts [9]. The dead-band of our Hewlett Packard 3457A Digital Multimeter is small enough for this effect to be negligible. There remains, however, the problem of the *stability* of the detector-digital voltmeter gain. The day-to-day gain varies by ~0.1% when the room temperature is controlled to ±1 °C. This instability contributes an estimated ±0.003 ppm type B uncertainty to the sample-resistor measurements because our reference resistors are about 2–3 ppm smaller than the quantum Hall resistance.

The 3×10^{12} Ω measurement system leakage resistance contributes an estimated ±0.002 ppm type B uncertainty.

No temperature-dependent [7] or current-dependent [8] quantized Hall resistance (QHR) corrections could be detected for the Hall-probe set used on this sample. The respective estimated type B uncertainties for the dependence of the QHR on temperature and current are ±0.002 ppm and ±0.001 ppm.

The total root-sum-square uncertainty is typically ±0.007 ppm. This uncertainty is only one third that of the old potentiometric measurement system [9] and the bridge system [9,10]. The smaller uncertainty owes to: a) the ability to directly interchange the sample and the reference resistor positions in the measurement system, rather than having to substitute another reference resistor for the sample in order to determine the interchange error; b) a smaller interchange error; c) the fact that there is only one uncorrelated uncertainty of the detector-digital voltmeter gain, rather than the three correlated uncertainties in the bridge system; and d) a larger leakage resistance.

6. Results

The United States legal unit of resistance Ω_{NBS} is being monitored via the quantum Hall effect [9], as outlined in steps 1 to 3 of section 1. Comparisons between R_H and R_R are made as part of this ongoing procedure. Figure 3 displays the current results. The value of the 6,453.20 Ω reference resistor

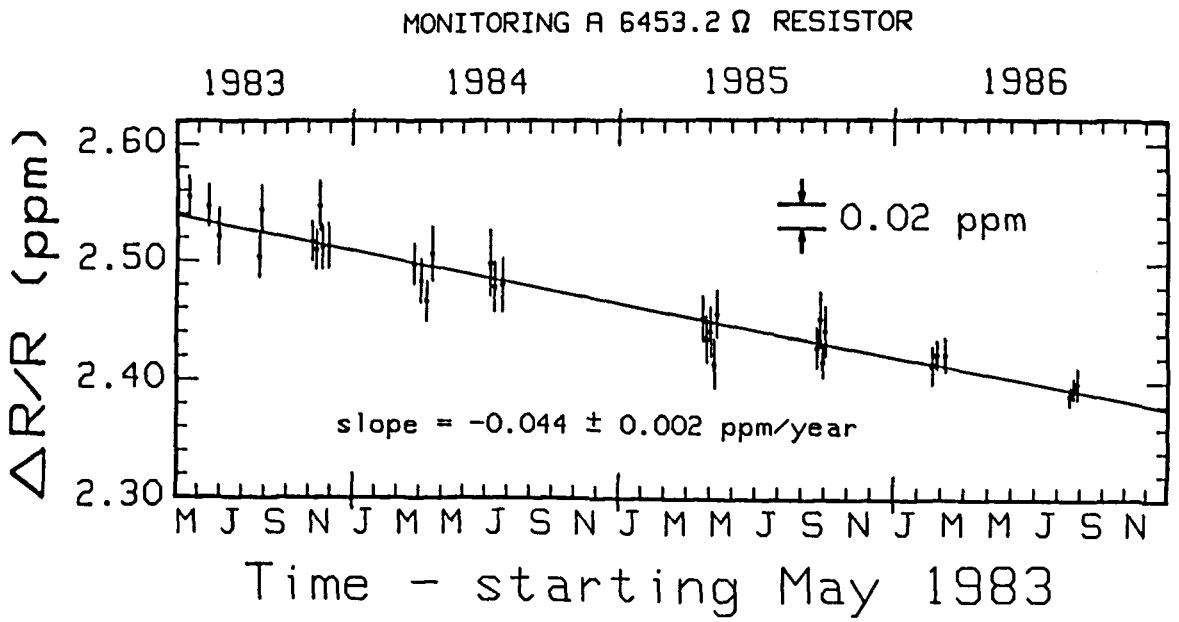

Figure 3-Relative comparisons as a function of time of the resistance of the $i=4$ steps of three different quantum Hall devices with that of a nominal 6,453.20 Ω wire-wound reference resistor. $\Delta R/R=(V_H-V_R)/V_R$. The value of this resistor is increasing by (0.044±0.002) ppm/year. The last set of data points were obtained with the new measurement system.

used in the comparisons is increasing by (0.044±0.002 ppm/year). The August 1986 data shows the improved measurement accuracy of the new automated potentiometric system over that of the old, manually-operated potentiometric measurement system and the automated bridge system. This new measurement system has proved to be quite reliable, very flexible, and easy to use.

The authors acknowledge having had useful discussions with, and receiving helpful suggestions from, C. T. Van Degrift, T. E. Kiess, B. F. Field, and R. F. Dziuba of the Electricity Division of NBS. One of the authors (G. M. R.) is especially grateful to B. N. Taylor for the opportunity to work on the quantum Hall effect in the NBS Electricity Division.

References

[1] v. Klitzing, K.; G. Dorda and M. Pepper, New method for high accuracy determination of the fine-structure constant based on quantized Hall resistance, Phys. Rev. Lett. **45** 494 (1980).

[2] Tsui, D. C., and A. C. Gossard, Resistance standard using quantization of the Hall resistance of GaAs/AlGaAs heterostructures, Appl. Phys. Lett. **38** 550 (1981).

[3] Delahaye, F.; D. Dominguez, F. Alexandre, J. P. Andre, J. P. Hirtz, and M. Razeghi, Precise quantized Hall resistance measurements in GaAs/$Al_xGa_{1-x}As$ and $In_xGa_{1-x}As$/InP heterostructures, Metrologia **22** 103 (1986).

[4] v. Klitzing, K., and G. Ebert, Application of the quantum Hall effect in metrology, Metrologia **21** 11 (1985).

[5] Taylor, B. N., Impact of quantized Hall resistance on SI electrical units and fundamental constants, Metrologia **21** 3 (1985).

[6] For an up-to-date collection of the measurement results from different laboratories see the Proceedings of the Conference on Precision Electromagnetic Measurements 1986, to be published in IEEE Trans. Instrum. Meas. **IM-36** (June 1987).

[7] Cage, M. E.; B. F. Field, R. F. Dziuba, S. M. Girvin, A. C. Gossard, and D. C. Tsui, Temperature dependence of the quantum Hall resistance, Phys. Rev. B **30** 2286 (1984).

[8] Cage, M. E.; R. F. Dziuba, B. F. Field, E. R. Williams, S. M. Girvin, A. C. Gossard, D. C. Tsui, and R. J. Wagner, Dissipation and dynamic nonlinear behavior in the quantum Hall regime, Phys. Rev. Lett. **51** 1374 (1983).

[9] Cage, M. E.; R. F. Dziuba, B. F. Field, T. E. Kiess, and C. T. Van Degrift, Monitoring the U.S. legal unit of resistance via the quantum Hall effect, IEEE Trans. Instrum. Meas. **IM-36** (June 1987, to be published).

[10] Field, B. F., A high-accuracy automated resistance bridge for measuring quantum Hall devices, IEEE Trans. Instrum. Meas. **IM-34** 2286 (1984).

Journal of Research of the National Bureau of Standards

The NBS Large-Area Alpha-Particle Counting Systems

Volume 92 Number 5 September-October 1987

J. M. R. Hutchinson,
S. J. Bright

National Bureau of Standards
Gaithersburg, MD 20899

Two alpha-particle counting systems for the measurement of large-area sources have been developed at the National Bureau of Standards. The systems and their characteristics are described. One system uses an internal-source proportional counter and the other measures sources external to the counting volume through a thin aluminized mylar window. The "internal" system is used to measure sources in the lower activity ranges. These calibrated sources are then used to establish the efficiency of the "external" counter used to measure the higher-activity sources.

Key words: alpha particle; large area; monitoring; proportional counting; radioactivity; standards.

Accepted: April 27, 1987

1. Introduction

Recently the National Bureau of Standards (NBS) has developed two alpha-particle counting systems for the calibration of large area sources. These internal-source and an external-source gas-proportional counting systems were requested by the United States Air Force (USAF) to calibrate large-area sources to serve as transfer standards between the USAF and NBS. The sources are rectangular, 8-in×5-in, with ^{238}Pu deposited on an aluminum substrate. The active area is an array of 1-mm diameter dots spaced a minimum of 4 mm apart. The four sources used range in total activity from 10^2 to 10^5 Bq.

Measurements described here have characterized the potential errors when calibrations are performed with the two systems, and when the calibrated sources are used to calibrate field monitoring equipment.

About the Authors: J. M. R. Hutchinson and S. J. Bright are with the Center for Radiation Research in NBS' National Measurement Laboratory.

2. Counting Systems

2.1 Internal Gas-Proportional Counter

The counter is pictured in figure 1 and shown schematically in figures 2a and 2b. A 13-in×9-in Herfurth large-area flow proportional counter HGZ 730-C is mounted on four aluminum pedestals. The various grills, safety grids, and aluminized-mylar-foil window are removed and replaced with a vertically movable baseplate which supports the source and seals the counting volume by means of an "O" ring. Pressure for the seal is applied by five clamps. A clamp was not mounted on one of the sides, thereby permitting easy insertion of the source on this side. The baseplate is moved up and down with a lab-jack which is driven by a small motor. The vertical excursions both at the top and bottom of the baseplate movement are limited by microswitches which cut off the motor when the baseplate presses on them. The baseplate is not attached to the lab-jack so that if the motorized downward motion of the jack were accidently activated while the clamps were closed, the baseplate would remain clamped to the rest of

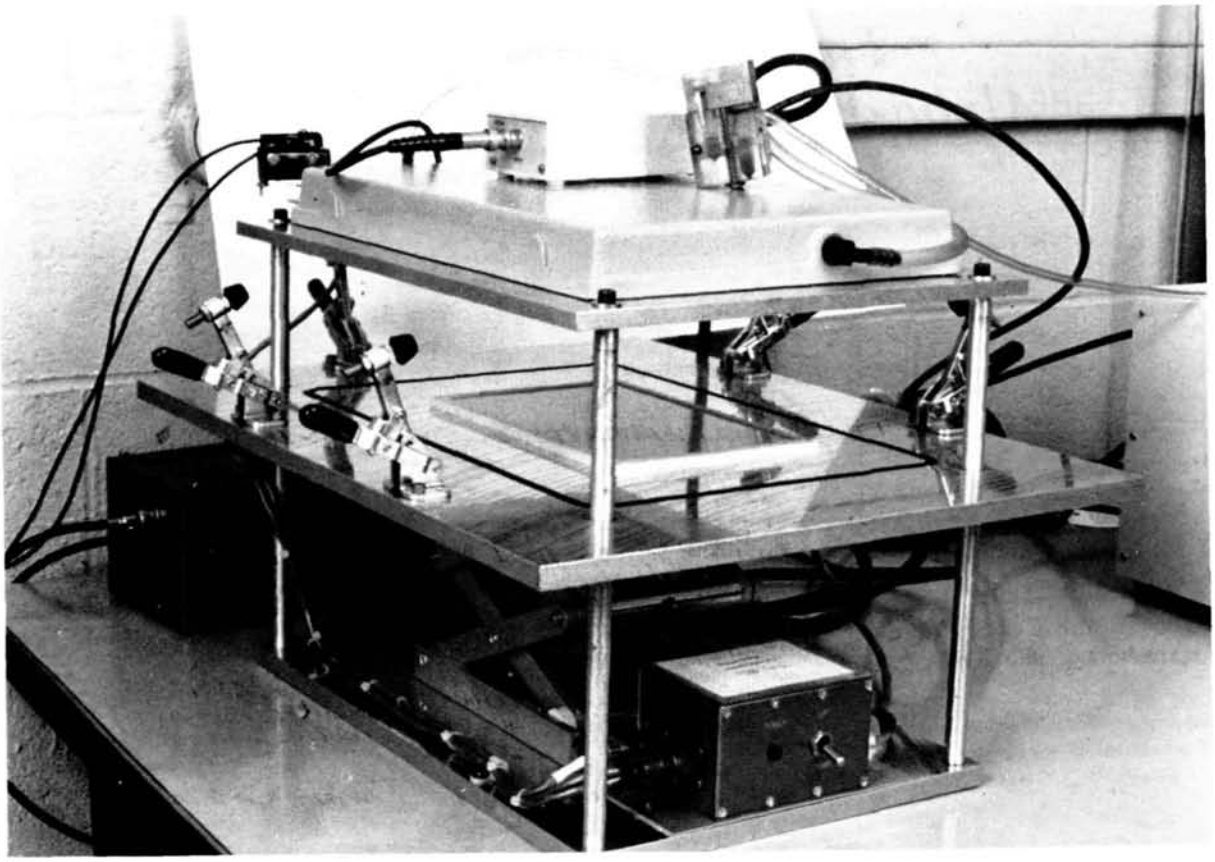

Figure 1–Internal 2π-alpha-particle gas-proportional counter with a large-area source in counting position. When counting, the baseplate is raised and the clamps are tightened.

the counter, the jack would move down alone, and no damage would result to the motor.

The normal counting gas is P-10 at atmospheric pressure. Typically it takes 2–3 minutes after the gas flow is turned on before the alpha-particle pulses reach full height. After that, the counting space is flushed at a rate of about a bubble through the bubbler per one or two seconds. The procedure for counting a source in this counter is given in the Appendix.

A schematic drawing of the electronics for this and the external counting system is given in figure 3. Pulses originating in the counting volume as a result of energetic alpha particles producing ions within the counter, with subsequent gas multiplication, are passed into a charge-sensitive preamplifier, then into an amplifier, and are recorded in a multichannel analyzer which is read out on tape for subsequent evaluation. The pulse-height spectrum can be monitored on the MCA screen.

The high voltage is applied through a circuit which cuts off whenever the upper limiting microswitch is not under pressure from the baseplate. This is a safety feature which makes it impossible for an operator to introduce a source into the counter while the counter wires are at high voltage.

2.2 'External' Gas Proportional Counter

The counter is pictured in figure 4 and shown schematically in figure 5. It is used to compare sources with activities too high for the internal counter with previously calibrated standards. This counter is of identical original design to the internal counter. However, the movable "baseplate" is replaced by an aluminized mylar window which is supported by a mounting plate, permanently attached. Baffles can be inserted to reduce count rates to acceptable levels for very active sources.

The large-area source is inverted and placed onto the mounting plate and this represents the counting position. In order to make accurate comparisons with standards in this counting geometry, it was necessary that the source-to-detector configurations be reproducible and also that the active layer be "thin" to the emitted alpha particles so that variations in distance from the counter would not affect the count rate significantly.

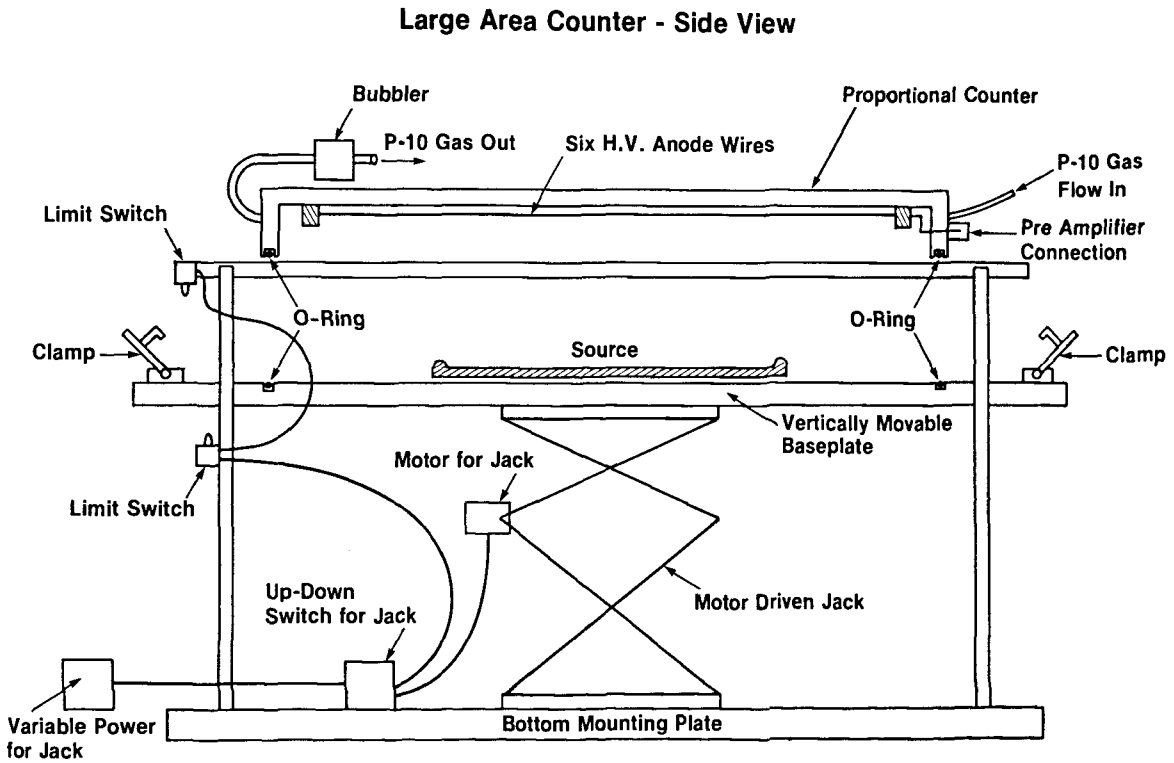

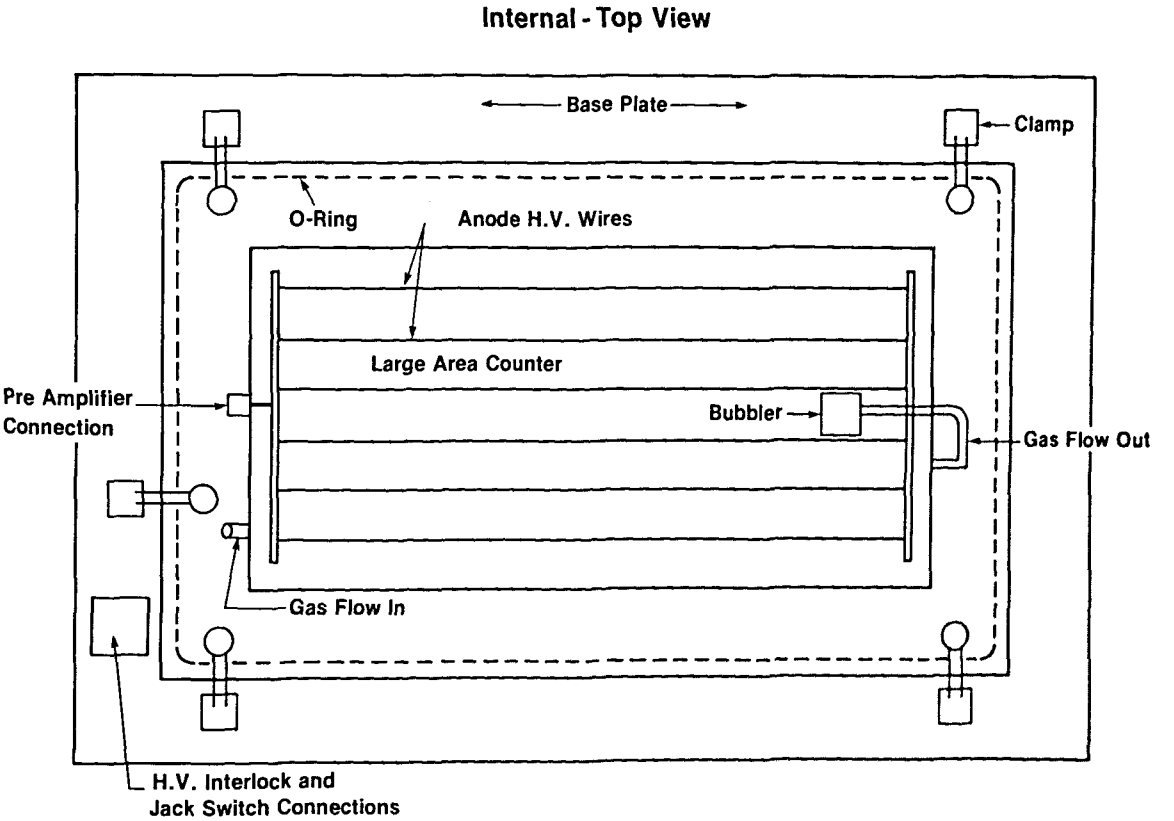

Figures 2a and 2b–Schematics of the internal gas-proportional counter. The detector has 19 anode wires with 1 cm separation (fig. 2b).

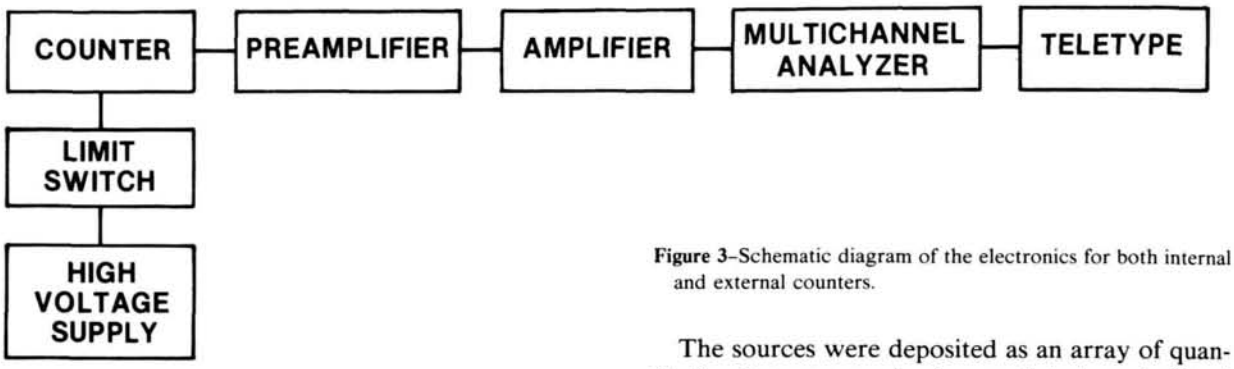

Figure 3–Schematic diagram of the electronics for both internal and external counters.

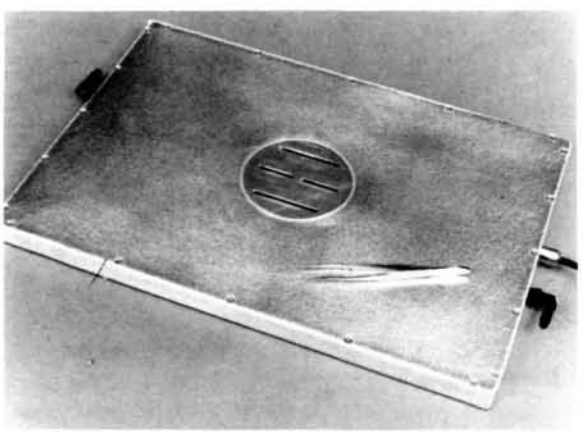

Figure 4–External-defined-aperture, thin-window, alpha-particle, gas-proportional counter with the slit baffle in place. The tweezers are used to remove the baffle carefully, so that the delicate mylar window is not damaged.

The expectation is that this source would provide a calibration device for essentially monoenergetic alpha particles for the monitoring instrument. The readout in a field measurement of surface contamination would be related to this calibration through a previously determined factor which would take into account alpha-particle absorption in the source. These factors are being developed into a forthcoming ISO standard.

3. Large-Area Sources

With this approach in mind, high-specific-activity ^{238}Pu rather than the relatively massive ^{239}Pu was chosen as the source nuclide. With this choice, sources could be provided in which the emitted alpha-particle peak taken, for example, with a surface barrier detector is clearly resolved (fig. 6).

The sources were deposited as an array of quantitative drops on an aluminum substrate and affixed by an anodizing process. A full scale radiograph of one of the sources is shown in figure 7. The active material is quite stable. For example, the results of a series of "swipe" tests show very little active material to be removed (table 1). Two sets of four sources ranging in total activity from 10^2 to 10^5 Bq were provided, one set to be retained by the USAF and one set to be kept at NBS.

The source size, easily accepted by the internal counter, was chosen because it was large enough to calibrate the present USAF monitoring instruments, AN/PDR-56F. Currently, the USAF calibrates these instruments with the AN/UDM-7C source sets. The new NBS large-area sources were designed to be compatible with retrofitting into the existing AN/UDM-7C jig in place of the existing sources which the USAF desires to replace. If the USAF should replace the AN/PDR-56F with another instrument in the future, the NBS large-area source design should be adaptable for that eventuality.

Table 1. "Swipe" tests of Pu-238 large area sources.

Source No.	Count Time (min)	Alpha Count	Beta Count	Alpha DPM	Beta DPM
AA373	1	25	3	49.8	3.0
AA372	1	17	5	33.8	7.0
AA371	1	3	0	5.8	−3.0
AA370	1	4	0	7.8	−3.0

4. Tests of the Counters

Figures 8 and 9 show the high voltage plateau for the internal and external counters, respectively. Clearly the adaptation from the external mode to internal produces little change in its functioning.

Figures 10a and 10b show the pulse-height spectra for the external counter for a 5 cm aperture for a large area source and for a point source. The two

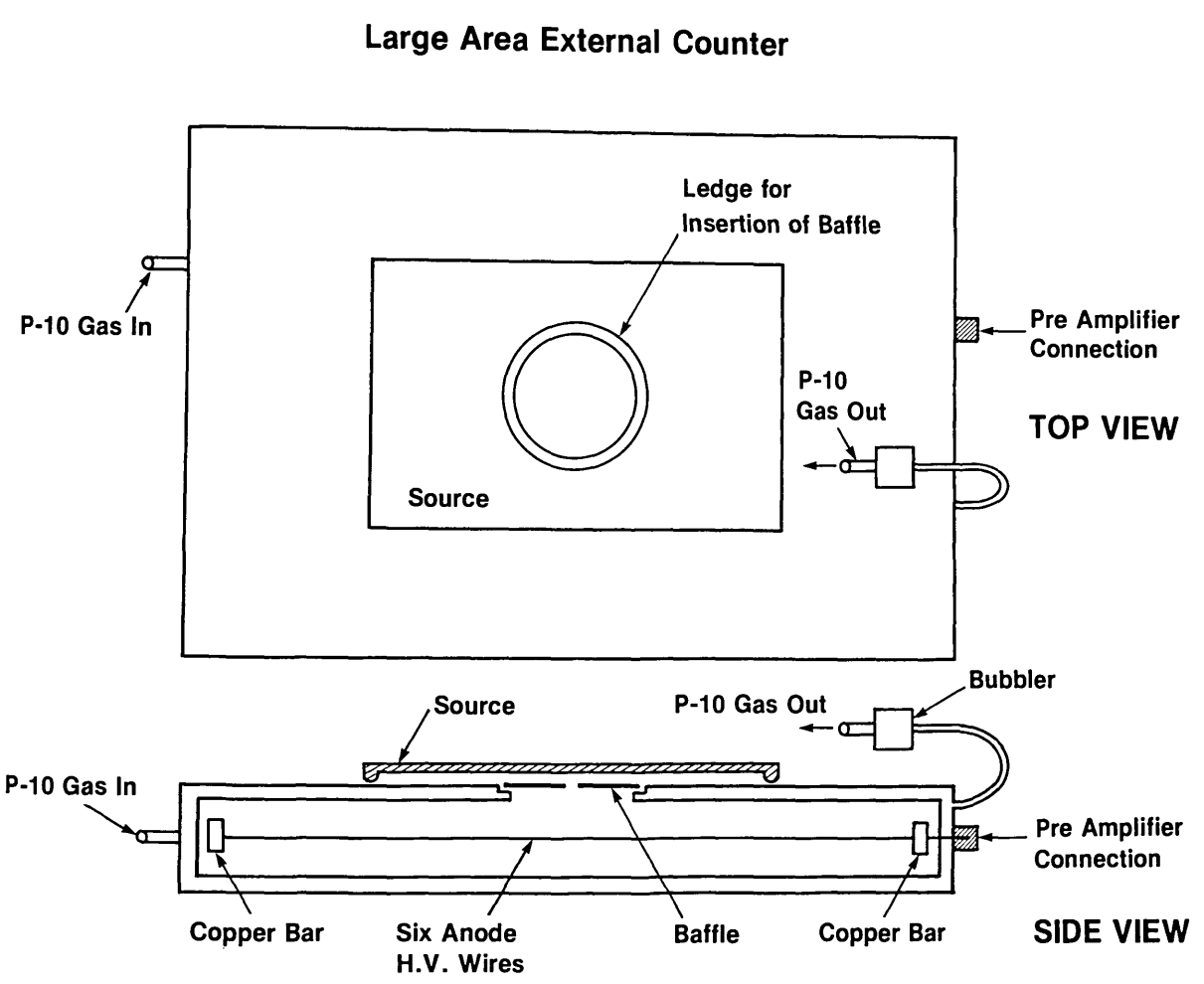

Figure 5–Schematic diagram of the external counter.

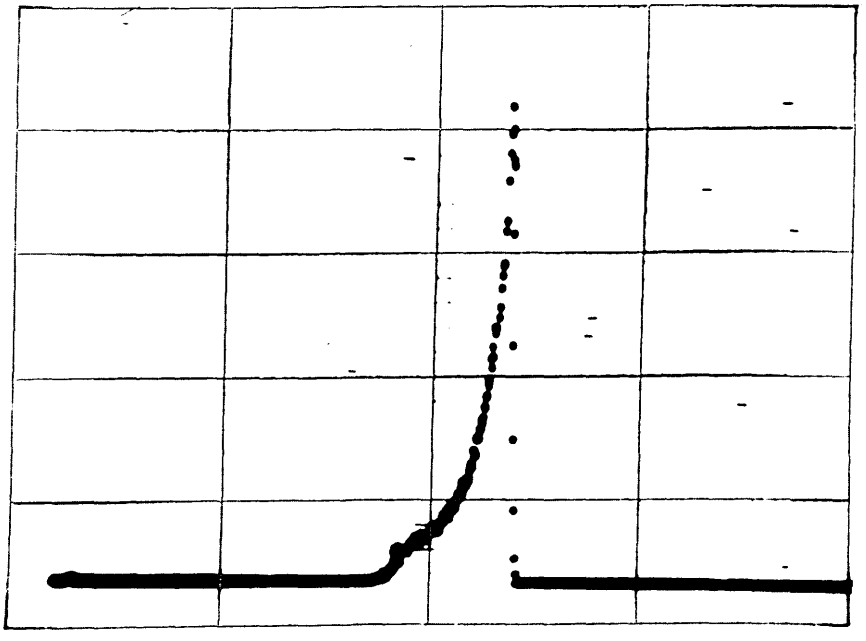

Figure 6–Silicon surface-barrier spectrum of the ^{238}Pu large-area sources. This shows that the peak to be well resolved, an important requirement in reducing systematic error in the calibration.

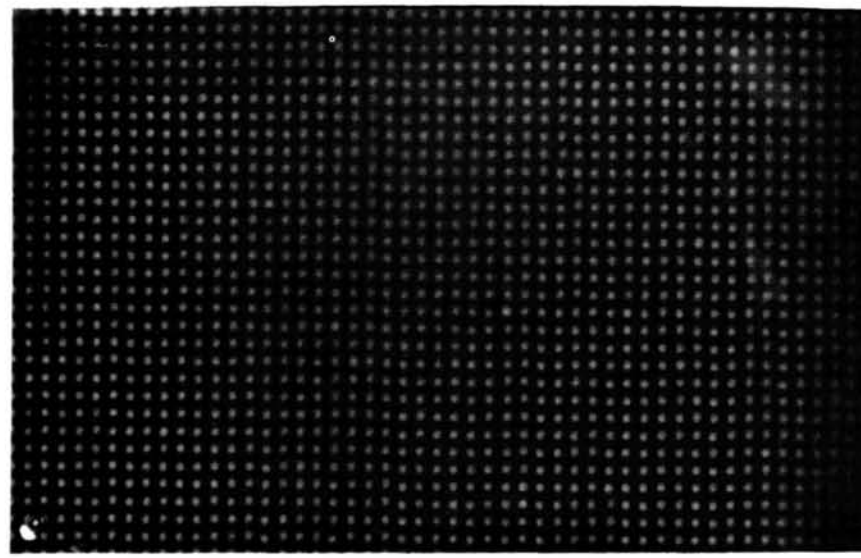

Figure 7–Radiograph of ^{238}Pu large-area source number AA373 full scale.

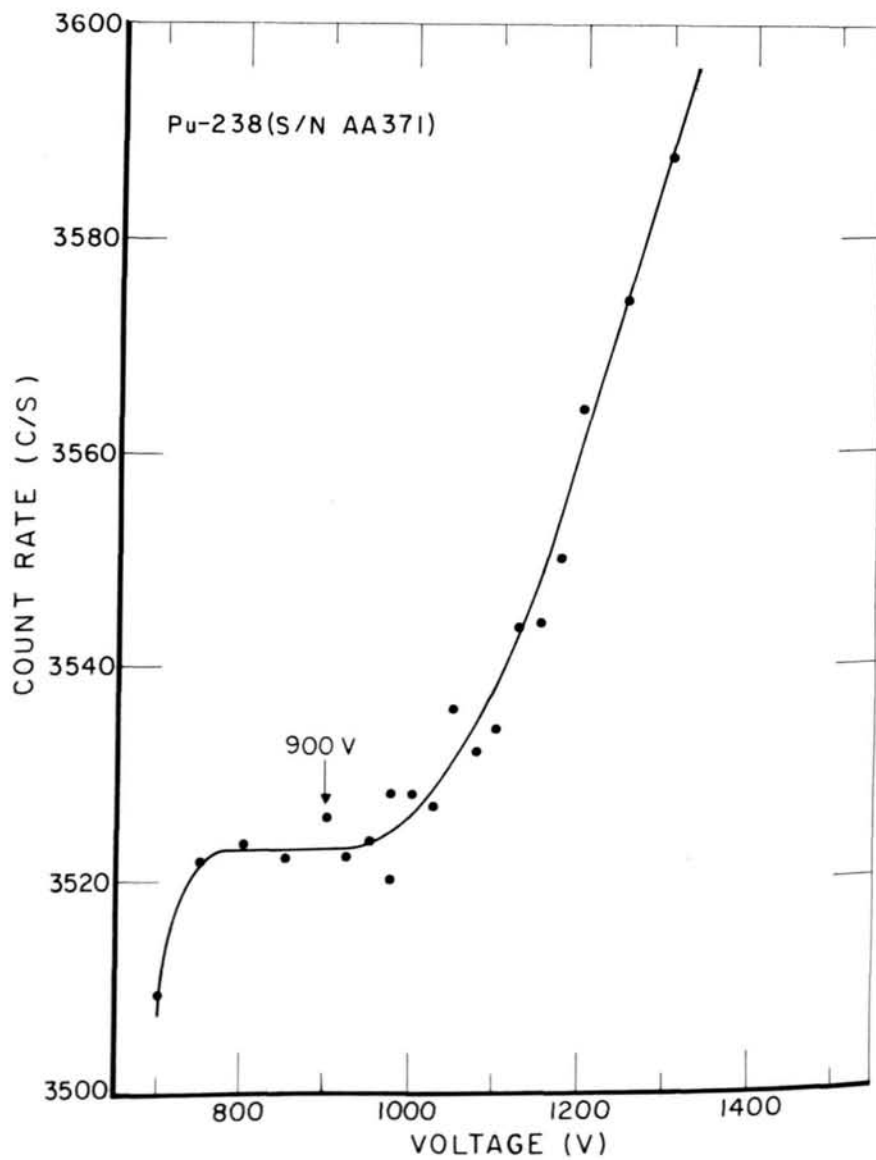

Figure 8–Voltage plateau of the large-area 2π-alpha-particle proportional counter using a large-area source. (Operating voltage was set at 900 V.)

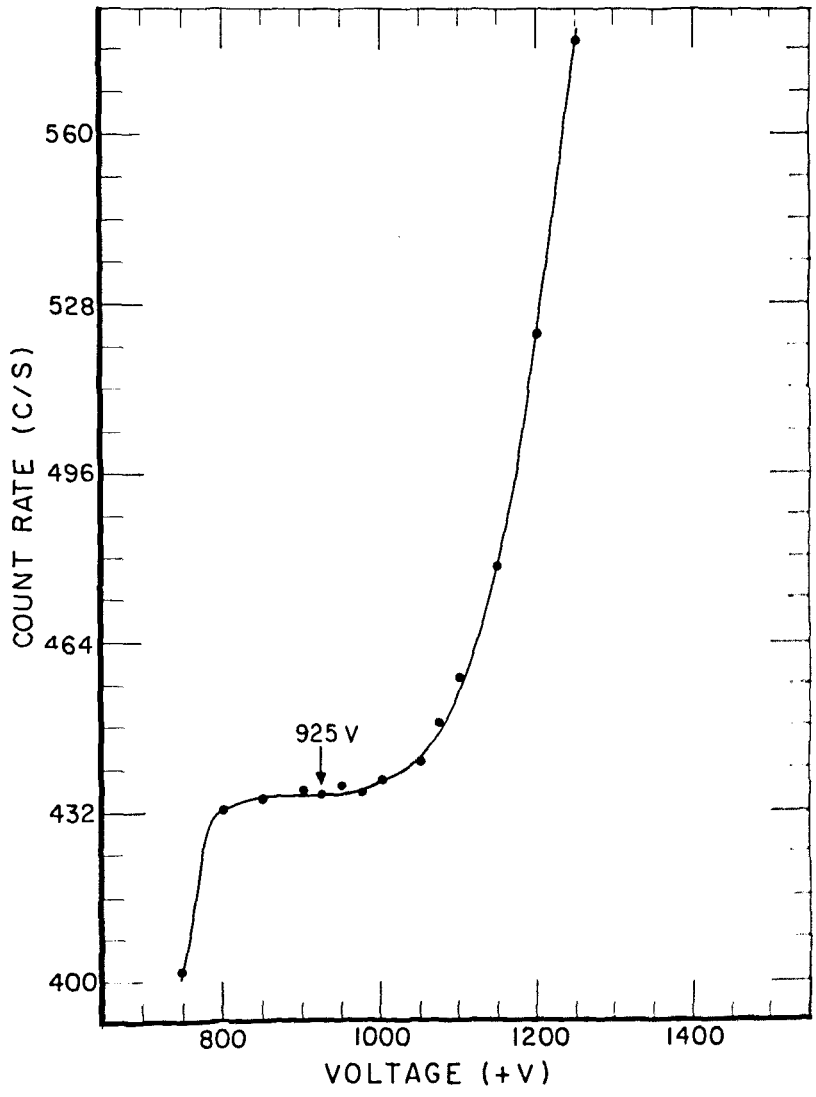

Figure 9–Voltage plateau of the external counter for a large-area ^{238}Pu source. (Operating voltage was set at 925 V.)

peaks do not represent different alpha-particle groups but rather result from different degrees of gas multiplication in different parts of the detector. Although we have not performed a thorough investigation of the effect, the initial direction of the alpha-particle relative to the anode wires affects the pulse height.

5. Homogeneity Tests Of the Superficial Activity Of the Sources

It is important that the activity deposits be homogeneously distributed over the source. The instrument reads, and will be calibrated, in terms of activity per square centimeter. The calibration is performed by placing the instrument over some part of the source and recording the readout which then represents the superficial activity value for the standard.

It is also important that uncertainties in the source-to-detector distance cause minimal uncertainty in the calibration. This is achieved by making the active deposits as thin as possible so that energy loss in the source is small. With a thick source, variations in the calibration position could introduce enough intervening energy-absorbing air mass to remove a significant number of degraded energy alpha particles from detection. For a thin source, reasonable changes in the air mass between source and detector merely reduce the full energy of the monoenergetic alpha particles which are nevertheless detected.

Experiments were performed to test both the homogeneity of the superficial activity and the response of the external detector and the AN/PDR-56F, as a function of source-to-detector distance. The homogeneity was tested using the external counter with no baffle (i.e., an aperture of 7 cm). Source positions relative to the aperture are

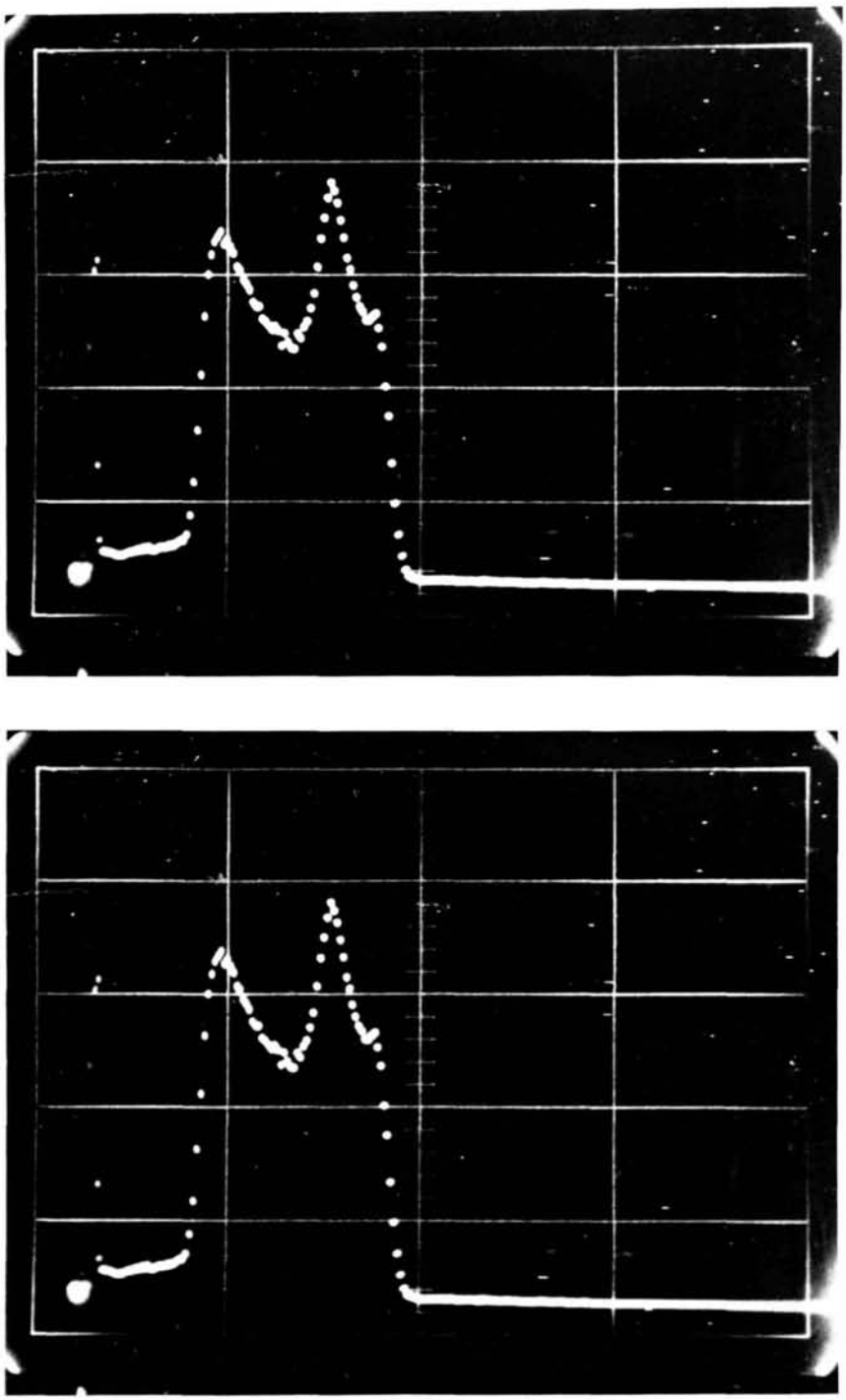

Figures 10a and 10b–Pulse-height spectra for the external counter for a large-area source using a 5-cm aperture (10a) and for a point source (10b).

given in figures 11a and 11b. Sources at each of the four activity concentration levels were tested with the results shown in table 2.

As seen in table 2, despite the fact that these are dried deposit sources, the maximum difference of any one of these readings is −6.3 percent from that of the center value. The maximum difference of average values relative to the center value is 1.021 or 2.1 percent. Presumably calibrations can be performed with an uncertainty from inhomogeneity on the order of 2 percent, since the calibration value is related to the average value.

Figure 12 shows the response of the external detector for two apertures, 1.3 cm and 7.6 cm in diameter, normalized to the largest value. For the larger aperture, as the source approaches the detector, the count rate approaches an asymptotic value. For the smaller aperture, the effect of the spot

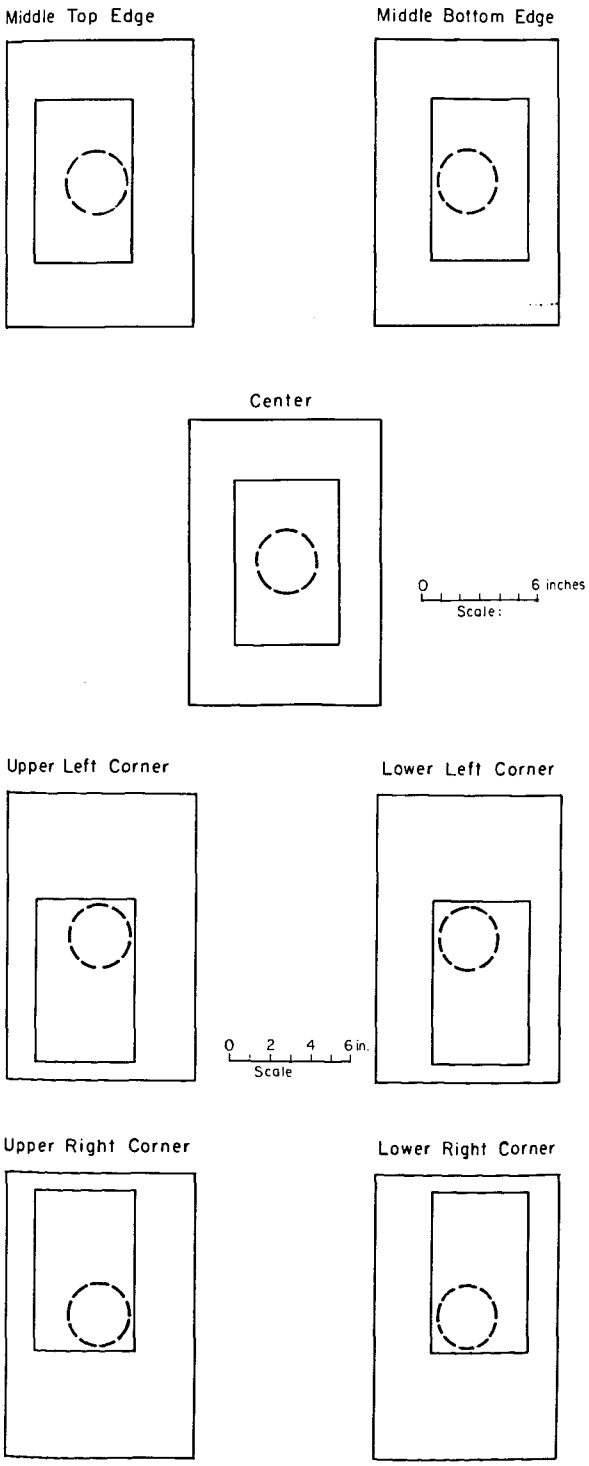

Figures 11a and 11b–Source positions relative to the aperture of the external counter to test the homogeneity of the large-area sources, with results given in Table 2.

character of the source manifests itself. The count rate goes through a maximum at a vertical distance of 3 mm, presumably because counts from adjacent spots are possible as the source moves away from the counter.

Another measure of the effect of vertical displacement of the source is shown in figures 13 and 14, measurements made with the AN/PDR-56F alpha-particle and x-ray probes, respectively. The alpha-particle probe is essentially a thin window plastic scintillation detector and the x-ray probe is a NaI(T1) scintillation device. The x-ray data demonstrate much less variation as a function of distance.

Since the relative positioning of an unknown and a comparison standard source is within 1 mm, the uncertainty due to source positioning, at vertical distances in figure 12 between 0 and 1 mm, is less than a few tenths of one percent.

Table 2. Results of tests using four concentration levels and eight source positions.

(Large Area External Detector #34152/Pu-238/No Baffle)

	Count Rate Divided by Rate at the Center			
Area of Source	Source No. AA371	Source No. AA370	Source No. AA841	Source No. AA840
Upper Left Corner	0.977	1.029	1.019	1.025
Lower Left Corner	0.977	1.021	1.013	1.024
Upper Right Corner	1.017	0.943	1.010	1.062
Lower Right Corner	1.033	0.937	1.016	1.021
Middle of Top	0.974	1.003	0.998	1.017
Middle of Bottom	1.003	0.980	0.967	0.977
Center	1.00	1.00	1.00	1.00
Average to Center	0.997	0.986	1.004	1.021

6. Calibration Procedure

The startup, source change, and shutdown procedures are given in the Appendix.

The radioactivity measurements of all four activity-level sources are based on 2π-internal-counter measurements of the two lower-activity sources. The two higher-activity sources produce count rates in the internal counter beyond the dynamic range of the system. Consequently, the external counter was calibrated with the two previously calibrated low-activity sources, and the two higher-activity sources then compared in the same geometry.

The total 2π-alpha-particle rates thus measured are given in the certificate, typical examples of which are shown in figures 15 and 16, using respectively, the internal and external counters for the calibration.

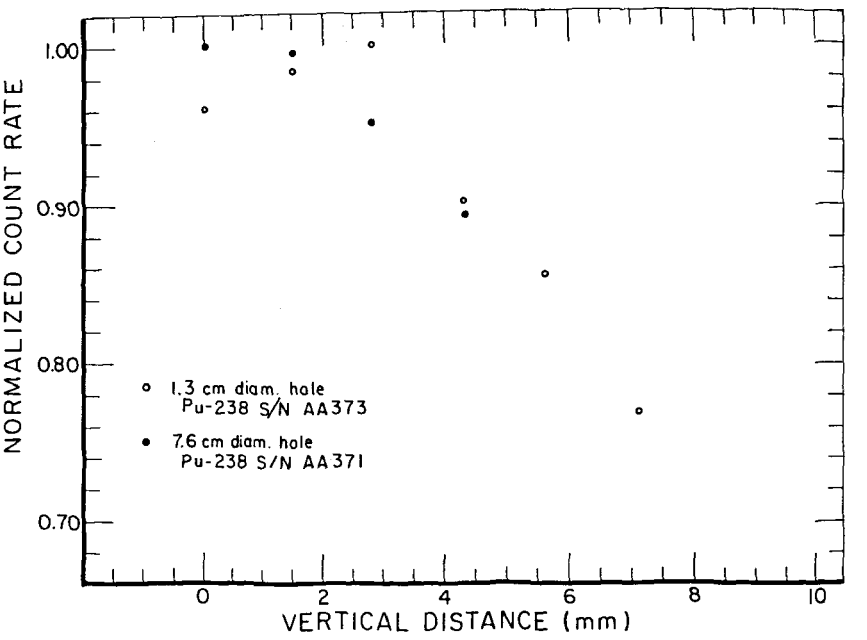

Figure 12-Count rate of a large-area ^{238}Pu source normalized to the largest value measured with the external counter versus distance from the external counter. Zero distance corresponds to the source resting on the counter top (supported by the edges of the source). The distance from the active layer to the sensitive volume is 2 mm.

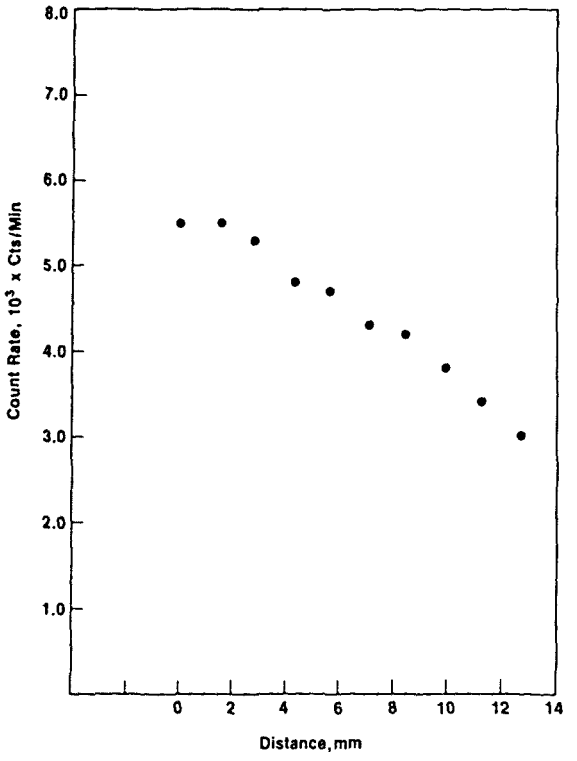

Figure 13-Count rate versus distance between a large area ^{238}Pu source and the face of a DT-224B/PDR-56 probe. The zero distance corresponds to the condition where the probe and source are mounted in the UDM-7 jig. The active area is separated from the sensitive volume by 7-mm at "0" distance.

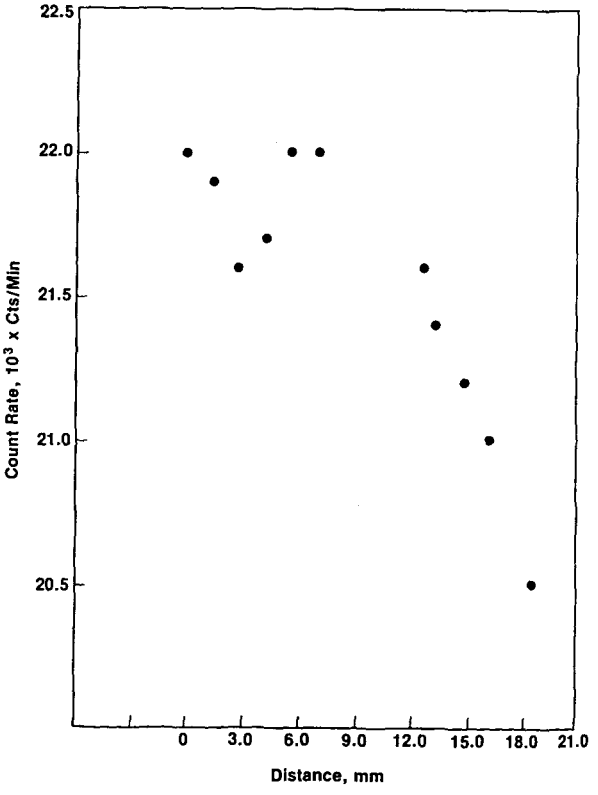

Figure 14-Count rate versus distance between a large area ^{238}Pu source and an x-ray probe, DT-590/PDR-56F. The zero distance corresponds to the condition where the probe and source are mounted in the UDM-7 jig. The active area is separated from the sensitive volume by approximately 16-mm at "0" distance.

FORM NBS-259
(REV 6-69)

U.S. DEPARTMENT OF COMMERCE
NATIONAL BUREAU OF STANDARDS
GAITHERSBURG, MARYLAND 20899

REPORT OF TEST

for

HQ Aerospace Guidance and Metrology Center
Newark Air Force Station, Ohio

Radionuclide	Plutonium-238
Source identification	#AA370
2π alpha-particle counting rate	$2.459 \times 10^3\ s^{-1}$ (1)*
Reference time	July 31, 1986
Overall uncertainty	1.5 percent (2)
Measuring instrument	Large-area, $2\pi\alpha$ proportional counter

For the Director,

Dale D. Hoppes, Group Leader
Radioactivity Group
Center for Radiation Research

Gaithersburg, MD. 20899
August 4, 1986

*Notes on next page

NOTES

(1) Including scattered alpha particles.

(2) The overall uncertainty is three times the value found from combining quadratically the standard deviations of the mean, or approximations thereof, of the following:

a)	One standard deviation of the mean of 11 measurements	0.07 percent
b)	Count-rate-vs-energy extrapolation to zero energy	0.50 percent
c)	System live time	0.05 percent

For further information contact J.M.R. Hutchinson or S.J. Bright at (301) 921-2396.

#AA370

Figure 15–Typical certificate for source measured with the internal counter, the report test document above and the notes at right.

Form NBS-199
(REV 8-85)

U.S. DEPARTMENT OF COMMERCE
NATIONAL BUREAU OF STANDARDS
GAITHERSBURG, MARYLAND 20899

REPORT OF TEST

for

HQ Aerospace Guidance and Metrology Center
Newark Air Force Station, Ohio

Radionuclide	Plutonium-238(1)*
Source identification	#AA372
2π alpha-particle counting rate	$3.798 \times 10^5\ s^{-1}$ (2)
Overall uncertainty	5.6 percent (3)
Reference time	September 4, 1986
Measuring method	Large-area, defined aperature, thin-window, proportional counter.

For the Director,

Gaithersburg, MD. 20899
September 29, 1986

Dale D. Hoppes, Group Leader
Radioactivity Group
Center for Radiation Research

*Notes on next page

NOTES

(1) Large area source of plutonium-238, 6-in x 9-in active area, in an aluminum oxide layer. The activity is distributed as a matrix of points approximately 0.4 mm from one point to the nearest point.

(2) Determined by comparison with a source previously calibrated by $2\pi\alpha$ particle proportional counting.

(3) The overall uncertainty is three times the value found from combining quadratically the standard deviations of the mean, or approximations thereof, of the following:

a)	One standard deviation of the mean of 5 measurements	0.02 percent
b)	Macroscopic inhomogeneity of the superficial activity	0.28 percent
c)	Count-rate-vs-energy extrapolation to zero energy	0.74 percent
d)	System live time	0.05 percent
e)	Uncertainty of the standard source previously calibrated by $2\pi\alpha$ counting	0.51 percent
f)	Vertical positioning	1.6 percent

For further information contact J.M.R. Hutchinson or S.J. Bright at (301) 921-2396.

#AA372

Figure 16–Typical certificate for source measured with the external counter, the report test document above and the notes at right.

The calibration procedure is as follows for counting with the 2π internal counter:

After the source has been introduced into the counter and the sensitive volume flushed until the pulses observed on the pulse-height analyzer have reached their maximum height, the counting procedure is initiated. Typically, the counting proceeds in the order: background, standard reference source, submitted source, standard reference source, background. The counting times are adjusted so that 10^6 counts from the source are collected (corresponding to 0.1 percent statistical uncertainty). These counts are collected usually over five counting periods, with approximately 2×10^5 counts per measurement.

The functioning of the instrument is checked by comparing the measurement results for the standard, corrected for decay, and the background with previous results.

Five pulse-height windows are set covering the lower end of the spectrum for the purpose of obtaining an extrapolation in the case where the total number of counts into 2π are required. The extrapolation is based on the approximation that the "true" tail of the spectrum can be represented as a flat horizontal line with a height corresponding to the spectrum minimum. Background is subtracted and the result, reduced to counts per second, is entered onto the calibration certificate. The MCA automatically corrects for system "dead time" if run on "live time". The random uncertainty is taken as the internal standard deviation of the mean of the five repetitions with a total of 10^6 counts. The corresponding random uncertainty would be 0.1 percent if other components of variation are all zero. A comparison of the internal standard deviation and, in this case, 0.1 percent is referred to as the "index of dispersion" test. Other uncertainties are estimated at the 1σ level and are added in quadrature. The overall uncertainty quoted in the certificate is three times the calculated combined uncertainty.

For comparison of a source previously calibrated in the internal counter with another (usually "hotter") source using the "external" counter, a similar procedure is followed except that the known and unknown sources are counted alternately. The center of each source is placed over the aperture. As previously described (see table 2), uncertainties due to inhomogeneity average out to a large extent when count rates are referred to the central part of the source.

Appendix

1. Operation of Large-Area Internal Counter

A. To Start

•Set up system (Connect H.V. supply, amplifier, preamplifier, H.V. interlock box and gas-flow indicator).

•Turn on electronics (NIM BIN), interlock box and power supply for the jack.

•With clamps released, lower the bottom plate of counter by placing switch in "down" position.

•Place source in center of counter, handling source with gloves to prevent contamination.

•Raise by placing switch in "up" position.

•After counter is closed, tighten clamps.

•Turn on gas (P-10, Argon-Methane) at main valve and adjust diaphragm control to flush rapidly for 10 minutes. NOTE: Do not exceed 2–3 psi (F=PA, where with a large area the force must be controlled by a small gas pressure). Turn on high voltage (+925 V) at start of flushing.

•After flushing, adjust regulator to produce a gentle gas flow.

•Connect amplifier to oscilloscope and observe pulses, usually with a coarse gain of 500, positive input, and bipolar output.

•Connect amplifier to analyzer, set summing regions, and collect data.

B. To Change Source

•Turn off H.V. and gas flow.

•Release clamps, lower counter, and change source.

•Raise counter and tighten clamps.

•Flush counter, turn on H.V.

•Observe pulses and collect data.

C. To Shut Down

•Turn off electronics (NIM BIN).

•Turn off gas (close main valve and release the diaphragm).

•Remove source or blank.

•Close counter.

•Turn off H.V. interlock box and power supply for the jack.

•Take smears of counter and immediate area and count at Health Physics.

2. Operation of Large-Area External Counter

A. To Start

•Set up system (Connect H.V. supply, amplifier, preamplifier, and gas-flow meter).

•Turn on electronics (NIM BIN).

•If desired, place appropriate baffle in detector face.

•Place source in a defined position on the detector, handling source with gloves to prevent contamination.

•Turn on gas (P-10, Argon-Methane) at main valve and adjust diaphragm control to 2–3 psi. Open regulator and flush rapidly for 10 minutes. Turn on high voltage (+95 V) at start of flushing.

•After flushing, adjust regulator to produce a gentle gas flow (~60 cc/min).

•Connect amplifier to oscilloscope and observe pulses, usually with a coarse gain of 500, positive input, and bipolar output.

•Connect amplifier to analyzer, set integrals, and collect data.

B. To Change Source

•Simply remove source and change to different source, placing it at a defined position.

C. To Change Baffle

•Turn off high voltage and gas flow.

•Remove source.

•Remove baffle, putting tweezers in two small holes in the edge of baffle and lifing up. (Be careful not to tear the mylar.)

•Replace with appropriate baffle or no baffle, if desired.

•Place source on detector in defined position.

•Turn on gas and again flush for 10 minutes. Turn on high voltage at the start of flushing.

•Adjust regulator for a gentle gas flow.

•Observe pulses and collect data.

D. To Shut Down

•Turn off electronics (NIM BIN).

•Turn off gas (close main valve and release the diaphragm).

•Remove source or blank.

•Cover the thin-window aperture with the solid baffle.

•Take smears of counter and immediate area and count at Health Physics.

Journal of Research of the National Bureau of Standards

Mössbauer Imaging

Volume 92 Number 5 September-October 1987

Stephen J. Norton

National Bureau of Standards
Gaithersburg, MD 20899

In a Mössbauer experiment, if a spatially-extended absorbing sample is rotated relative to a moving γ-ray source, lines of constant γ-ray Doppler shift are generated through the absorber parallel to the motion of the source. As a result, resonant absorption takes place along a series of parallel lines cutting through the absorber, where a particular line is determined by the velocity of the source. The result is a series of measurements of line integrals of the absorption coefficient through the absorber. An image or spatial map of the absorption coefficient distribution may then be reconstructed using tomographic image-reconstruction algorithms. Moreover, when measurements are recorded both as a function of the source velocity and the absorber rotational velocity, spectral information may also be recovered as a function of position. Spatial resolution is proportional to the rate of rotation of the absorber, but is ultimately signal-to-noise limited.

Key words: image reconstruction; imaging; Mössbauer effect; Mössbauer imaging; Mössbauer tomography; tomographic image reconstruction; tomography.

Accepted: April 30, 1987

1. Introduction

The Mössbauer effect is an important spectroscopic tool in materials science [1,2][1]. In a typical Mössbauer experiment, γ-rays emitted by a radioactive source are allowed to impinge upon a sample of absorbing material; the transmitted or resonantly-scattered γ-rays are then subsequently detected (fig. 1). Thus, in a transmission experiment, a detector counts the number of γ-rays passing through the absorber, and in a scattering experiment the detector counts the γ-rays re-emitted after resonant absorption. The Mössbauer effect, or nuclear γ-ray fluorescence, is made possible by the recoilless emission and absorption of the γ-rays in nuclei embedded in a solid lattice. As a result, the resonant linewidths, relative to the γ-ray energy, are characteristically very narrow. Moreover, the resonant absorption can be "tuned" merely by moving the source at a small velocity relative to the absorber, which imparts some kinetic energy, or Doppler shift, to the γ-ray. Changes in source-absorber speeds as small as a few millimeters per second are often sufficient to destroy the resonance. In the conventional Mössbauer experiment, an absorption spectrum of the material under study is generated by moving the source relative to the absorber and counting the transmitted γ-rays (or resonantly-scattered γ-rays in a scattering experiment) as a function of the relative source-absorber velocity.

About the Author: Stephen J. Norton is with the Metallurgy Division of NBS' Institute for Materials Science and Engineering.

[1]Figures in brackets indicate literature references.

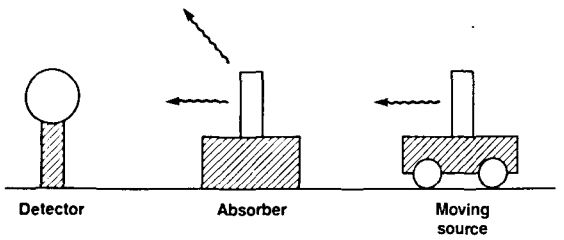

Figure 1-Conventional Mössbauer experimental arrangement with stationary absorber and moving source.

In this paper, we propose the idea of Mössbauer imaging. An image is by definition some quantity or parameter of interest displayed as a function of position, i.e., a picture of the parameter as it is distributed in space. In Mössbauer imaging, the simplest example of such a parameter is the Mössbauer absorption coefficient, and the aim would be to reconstruct and display its spatial distribution. A conventional Mössbauer experiment measures only a bulk average of the resonant absorption coefficient over the absorbing specimen. Thus, spatial inhomogeneities within an extended absorber, due either to variations in the absorption cross section of a pure material or to the mixture of different nuclei within a composite material, are inevitably averaged out in the bulk measurement process. A Mössbauer imaging experiment, however, would permit the reconstruction of a two-dimensional map of the Mössbauer absorption coefficient, that is, a two-dimensional picture of the strength of the resonant absorption as a function of position. In another, somewhat more complex, version of an imaging experiment, spectroscopic information as a function of position should also be recoverable, rather than merely differences in the absorption coefficient as a function of position. As a consequence, in the latter version, true Mössbauer spectroscopy can be performed in an imaging mode, so that heterogeneous or composite samples may be investigated.

The idea of Mössbauer imaging was inspired by the success of nuclear-magnetic-resonance (NMR) imaging, since NMR and the Mössbauer effect share some fundamental characteristics, both being nuclear resonance phenomena. NMR imaging has recently found notable success in diagnostic medicine [3]. While there are no foreseeable applications of Mössbauer imaging in medicine, applications to materials science are thought to exist. The ability to perform Mössbauer spectroscopy in an imaging mode, i.e., to do spectroscopy as a function of position within a sample, rather than in bulk, should prove to be of value in the analysis of heterogeneous materials. Although NMR and Mössbauer imaging may have different applications, it is instructive to compare the two techniques. In NMR imaging, resonant-frequency information is translated into spatial information by imposing a magnetic field gradient on a system of precessing nuclear spins. In Mössbauer imaging, we will see that by rotating the γ-ray absorber, a velocity gradient is imposed along the radial direction of the absorber and the resonance associated with a particular Doppler shift (analogous to a particular NMR precessional frequency) takes place along a family of lines perpendicular to the velocity gradient (analogous to the NMR magnetic field gradient). This process gives rise to a set of measurements of the line integrals of the absorption coefficient, from which an image can be recovered using well-known tomographic image reconstruction algorithms. These algorithms are mathematically similar to those employed in both x-ray and NMR tomography [4,5]. A more detailed description of the process by which the line-integral measurements arise is given in section 3.

The basis of the imaging approach can be most easily described using a classical interpretation of Mössbauer absorption, which will suffice for our purposes. As noted earlier, in this description the relative source-absorber velocity imparts a Doppler shift to the γ-ray. For purposes of illustration, consider the simplest case of a material with a single resonance line (neglecting isomer shifts); then resonance will take place at zero Doppler shift, or zero relative velocity between the source and absorber. By rotating an extended absorbing object relative to the source, lines of constant Doppler shift (or equivalently, of constant γ-ray energy) are generated across the absorber. As a result, resonant absorption takes place along one line at a time, giving rise to one line-integral measurement of the absorption coefficient. The location of the line is determined by three parameters: the absorber rotational velocity, the source velocity and the instantaneous position of the absorber during the measurement. From a complete set of such line-integral measurements, a spatial map of the γ-ray absorption can, in principle, be tomographically reconstructed. We shall see that the spatial resolution within the reconstructed image is proportional to the ratio of the natural linewidth of the resonance (in units of velocity) to the rate of rotation of the absorber, but is ultimately signal-to-noise limited. This means that, in principle, arbitrarily high resolution can be achieved, but at the expense of rapidly increasing detector integration times. In particular, the integration time will increase in direct proportion to the number of resolution elements (pixels) in the desired image. Thus, in a

two-dimensional image, doubling the linear resolution will square the number of pixels, which in turn will square the required integration time. As a consequence, very high resolution will require exceedingly long integration times unless sources of high intensity become more readily available.

At this stage one might observe that the equivalent line integral measurements could be generated merely by directing a collimated beam of γ-rays at the absorber over a wide range of incident angles. This approach is analogous to conventional x-ray computerized tomography in a transmission experiment or to single photon emission tomography in a scattering experiment. The advantage of the proposed method is that an extended source can be used rather than a collimated source, which implies a substantially greater incident γ-ray flux and a corresponding enhancement in the signal-to-noise ratio.

In the following three sections, we consider the idealized case of the γ-rays incident parallel to the x-axis. This can be achieved by moving the source sufficiently far away so that the source subtends a small angle at the absorber. The assumption of parallel incidence simplifies the analysis considerably and permits an analytical solution to the image reconstruction problem; it also allows the analytical inversion of the complete Mössbauer spectrum at each point (section 3). Moreover, the parallel-incidence case also permits the closed-form derivation of the image point spread function, which is defined as an image of a point object (Dirac delta function) and characterizes the resolving power of the imaging technique (section 4). In section 5 we consider an extended source which gives rise to γ-rays incident over a range of directions that are no longer parallel. In the latter case, the image reconstruction cannot be inverted analytically as for parallel incidence, but the reconstruction can nonetheless be performed using iterative algebraic reconstruction techniques [4,5]. Although such iterative reconstruction methods often fail to provide the insight and intuition of analytical solutions (which permit, for example, the closed-form derivation of the image point spread function), such methods are often more flexible in incorporating *a priori* information into the inversion algorithm. An important example is the incorporation of γ-ray attenuation due to a variety of scattering and absorption (resonant and nonresonant) mechanisms. For relatively thick objects, attenuation can no longer be ignored in the inversion. For the sake of tractability, we will, however, ignore attenuation in the next several sections.

2. Standard Experiment

Suppose a γ-ray emitted by a moving source is incident on a two-dimensional stationary absorber (fig. 2). For our purposes, it will suffice to describe the resonant absorption classically by modeling the

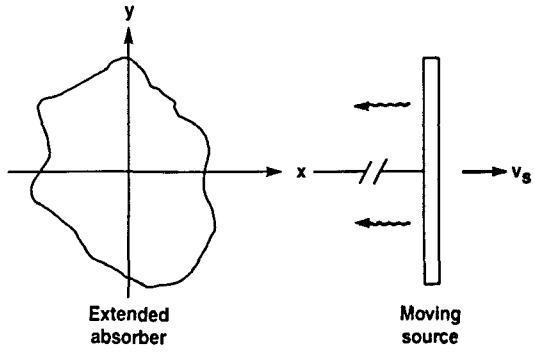

Figure 2–Two-dimensional absorber and distant moving source providing parallel γ-ray illumination.

nuclear resonance phenomenon, within a single absorbing nucleus, as a harmonic oscillator characterized by resonance frequency ω_a and linewidth τ (analogous to the mean lifetime of the γ-ray energy level) and driven by the electromagnetic field of the incident γ-ray. Letting $A(t)$ denote the response of this elemental oscillator, we have

$$\ddot{A}(t)+\frac{1}{\tau}\dot{A}(t)+\omega_a^2 A(t)=A_{inc}(t), \tag{1}$$

where

$$A_{inc}(t)=A_0 \exp\left[i\omega_0\left(1-\frac{v_s}{c}\right)t\right] \tag{2}$$

is the γ-ray electromagnetic field. In eq (2), v_s is the velocity of the moving source, c is the velocity of light and A_0 is a constant. Although one might also choose to include a finite linewidth in the γ-ray field $A_{inc}(t)$, we shall, for mathematical simplicity, lump all linewidth effects into the parameter τ in eq (1). Note that $\omega_0 v_s/c$ in eq (2) is just the classical Doppler shift due to the motion of the source. In an equivalent notation, $\omega_0=E_0/\hbar$ and $\Gamma=\hbar/\tau$, where E_0 is the energy of the incident γ-ray and Γ is the (energy) linewidth. Now in eq (1), set

$$\omega_a=\omega_0\left(1-\frac{v_a}{c}\right), \tag{3}$$

where v_a is a parameter (in units of velocity) that allows for shifts in the nuclear resonance of a given

nucleus. Thus, the "intrinsic velocity," v_a, is characteristic of different absorbing nuclei (or their environment). We will later allow v_a to vary with position. The solution of the differential eq (1) on substituting eq (2) is

$$A(t)=\frac{A_0 e^{i\omega_s t}}{\omega_a^2-\omega_s^2+i\omega_s/\tau}, \tag{4}$$

where

$$\omega_s \equiv \omega_0\left(1-\frac{v_s}{c}\right) \tag{5}$$

is the Doppler-shifted source frequency. Substituting eqs (3) and (5) into eq (4), and assuming v_s and $v_a << c$, eq (4) becomes

$$A(t)=\frac{A_0}{2\omega_0}\frac{e^{i\omega_s t}}{(v_s-v_a)\omega_0/c+i/2\tau}.$$

Classically, the intensity of the re-emitted γ-ray is proportional to $|A|^2$, i.e.,

$$I(v_a-v_s)\equiv|A|^2 = \left(\frac{A_0}{2\omega_0}\right)^2\frac{1}{(v_a-v_s)^2(\omega_0/c)^2+(1/2\tau)^2}, \tag{6}$$

or, in an equivalent notation,

$$I(v_a-v_s)=\left(\frac{A_0}{2\omega_0}\right)^2\frac{\hbar^2}{(v_a/c-v_s/c)^2E_0^2+\Gamma^2/4},$$

which is the familiar Lorentzian (or Breit-Wigner) distribution [1,2].

Because the detection of the re-emitted γ-ray is an incoherent process, we can regard eq (6) as proportional to the probability of the γ-ray re-emission as a function of the velocity difference $v=v_a-v_s$. To make eq (6) a valid probability density function in v, normalize eq (6) to have unit area when integrated with respect to v, i.e., define

$$P^{(\tau)}(v)\equiv\frac{2\omega_0^3}{\pi\tau A_0^2 c}I(v)=\frac{v_\tau/\pi}{v^2+v_\tau^2}, \tag{7}$$

where

$$v_\tau \equiv c/2\omega_0\tau$$

is the linewidth in units of velocity. From eq (7),

$$\int_{-\infty}^{\infty} P^{(\tau)}(v)\,dv = 1.$$

One can also show that

$$\lim_{v_\tau\to 0} P^{(\tau)}(v)=\delta(v), \tag{8}$$

where $\delta(\cdot)$ is the Dirac delta function.

Now let $\sigma(x, y, v_a)$ denote the resonant absorption cross section as a function of space and the intrinsic velocity v_a. Then the expected number of counts, denoted by $f^{(\tau)}(v_s)$, is proportional to the function $\sigma(x, y, v_a)$ weighted by the probability density function $P(v_a-v_s)$ and integrated over v_a, and all space:

$$f^{(\tau)}(v_s)=\iiint dx\,dy\,dv_a\,\sigma(x, y, v_a)P^{(\tau)}(v_a-v_s). \tag{9}$$

In this and subsequent integrals, we shall assume that the limits of integration are from $-\infty$ to $+\infty$ unless otherwise indicated. We can assume this by defining functions such as $\sigma(x, y, v_a)$ to be zero outside their support (i.e., beyond the boundaries of the absorber and the domain of v_a, and so on). Now, for convenience, suppose we temporarily consider the limit of very small v_τ (narrow resonant linewidth). As v_τ goes to zero, the probability density function $P^{(\tau)}(v_a-v_s)$ becomes highly peaked about $v_a=v_s$, and in the limit $v_\tau\to 0$, we can use eq (8) in (9). Thus, defining

$$f(v_s)\equiv\lim_{v_\tau\to 0} f^{(\tau)}(v_s),$$

we have from eqs (8) and (9),

$$f(v_s)=\iint dx\,dy\,\sigma(x, y, v_s),$$

which is the expected result for the standard Mössbauer experiment, that is, $f(v_s)$ is the absorption cross section evaluated at $v_a=v_s$ averaged over the sample.

3. Imaging with Parallel γ-Ray Incidence

Now let the absorber rotate clockwise about the z-axis at constant angular velocity Ω. Let (x, y) denote a stationary coordinate system and let (x', y') denote a moving coordinate system embedded in the rotating absorber, as illustrated in figure 3. At $t=0$, let the stationary (x, y) and the rotating (x', y') coordinate systems coincide; at this instant denote the absorber's cross-section function by $\sigma_0(x, y, v_a)$. For $t>0$, the absorber has rotated through an angle Ωt. Define $\sigma_t(x, y, v_a)$ as the ab-

sorption cross section relative to the stationary axes (x, y) at time t; then

$$\sigma_t(x, y, v_a)=\sigma_0(x', y', v_a), \tag{10}$$

where

$$x'=x\cos\Omega t-y\sin\Omega t \tag{11a}$$

$$y'=x\sin\Omega t+y\cos\Omega t, \tag{11b}$$

or, inverting,

$$x=x'\cos\Omega t+y'\sin\Omega t \tag{12a}$$

$$y=-x'\sin\Omega t+y'\cos\Omega t. \tag{12b}$$

Again consider a γ-ray incident parallel to the x-axis from a source moving at velocity v_s in the positive x-direction (fig. 3). Resonant absorption

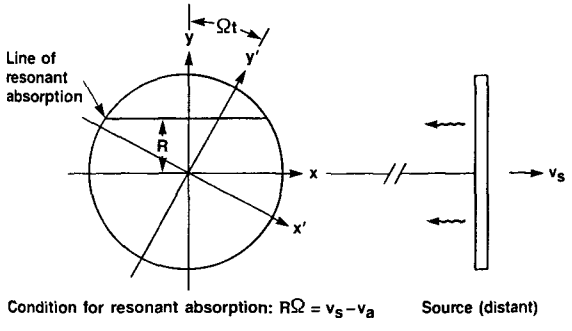

Figure 3–Rotating two-dimensional absorber with parallel γ-ray illumination. Resonant absorption takes place only along a line of "sensitivity" parallel to the x-axis at height R, where R is defined by the condition $R\Omega=v_s-v_a$.

will then take place when the total velocity v_a+v_a' of a point on the absorber equals the source velocity v_s, where v_a is the intrinsic material "velocity" and v_a' is the additional velocity contribution due to the motion of the absorber. Since the γ-ray is incident parallel to the x-axis, v_a' will be the x-component of the absorber velocity; thus, from eq (12),

$$v_a'=\dot{x}=\Omega y.$$

Note that v_a' depends only on y, so that resonant absorption takes place along lines parallel to the x-axis. For the stationary absorber, the resonance condition was $v_a=v_s$; for the rotating absorber, the resonance condition is modified to read

$$v_a+\Omega y=v_s. \tag{13}$$

Thus, for specific values of Ω and v_s, resonant absorption takes place along a line at height $y=(v_s-v_a)/\Omega$ parallel to the x-axis (fig. 3).

Now, in view of eq (13), for the rotating absorber, we can replace v_s in eq (9) by $v_s-\Omega y$, giving

$$f_t^{(\tau)}(v_s, \Omega)=\iiint dx\,dy\,dv_a\sigma_t(x, y, v_a)\cdot P^{(\tau)}(v_a-v_s+\Omega y). \tag{14}$$

Now considering a very narrow resonance, we again take the limit $v_\tau\to 0$. Defining

$$f_t(v_s, \Omega)\equiv\lim_{v_\tau\to 0} f_t^{(\tau)}(v_s, \Omega),$$

and using, from eq (8),

$$\lim_{v_\tau\to 0} P^{(\tau)}(v_a-v_s+\Omega y)=\delta(v_a-v_s+\Omega y)=\frac{1}{\Omega}\delta[y-(v_s-v_a)/\Omega]$$

in eq (14), we have

$$f_t(v_s, \Omega)=\frac{1}{\Omega}\iint dx\,dv_a\sigma_t[x, (v_s-v_a)/\Omega, v_a]. \tag{15}$$

This is our fundamental equation from which we shall solve for the function $\sigma_0(x', y', v_a)$ from the data $f_t(v_s, \Omega)$ recorded as a function of v_s, Ω, and t. Below, we consider four special cases of increasing generality: 1) one-dimensional imaging with no v_a distribution (i.e., assuming a single spectral line at $v_a=0$); 2) two-dimensional imaging with no v_a distribution; 3) one-dimensional image with an arbitrary and unknown v_a distribution; and finally 4) two-dimensional imaging with an arbitrary and unknown v_a distribution.

One-Dimensional Imaging with No v_a Distribution. We consider the simplest imaging case here. Suppose the absorber is one-dimensional and rotating. For convenience, assume the absorber is aligned with the (rotating) y'-axis, and suppose further that the measurements are made at the instant the absorber rotates past vertical, i.e., when the rotating absorber coincides with the y-axis at $t=0$. We then have

$$\sigma_t(x, y, v_a)=\sigma_0(y)\delta(x)\delta(v_a).$$

and eq (15) reduces to the simple result

$$f_0(v_s, \Omega)=\frac{1}{\Omega}\sigma_0(v_s/\Omega).$$

Thus, the spatial dependence of the one-dimensional cross section $\sigma_0(y)$ is given explicitly as a function of v_s/Ω.

Two-Dimensional Imaging (Tomography) with No v_a Distribution. Here we let

$$\sigma_t(x, y, v_a)=\sigma_t(x, y)\delta(v_a), \tag{16}$$

so that eq (15) becomes

$$f_t(v_s, \Omega)=\frac{1}{\Omega}\int dx\,\sigma_t(x, v_s/\Omega). \tag{17}$$

Recall that the measurements $f_t(v_s, \Omega)$ are made as a function of time as the absorber rotates. To make the t-dependence in eq (17) explicit, rewrite eq (17) as follows.

$$f_t(v_s, \Omega)=\frac{1}{\Omega}\iint dx\,dy\,\sigma_t(x, y)\delta(y-v_s/\Omega)$$

$$=\frac{1}{\Omega}\iint dx'dy'\sigma_0(x', y')$$

$$\cdot\delta(-x'\sin\Omega t+y'\cos\Omega t-v_s/\Omega), \tag{18}$$

where eqs (10) and (12b) were used in the last step. From eq (18), $f_t(v_s, \Omega)$ is a line integral through the two-dimensional function $\sigma_0(x', y')$ along a line parameterized by the radial distance v_s/Ω and the angle Ωt from the y'-axis. The inversion of eq (18) for $\sigma_0(x', y')$ can be carried out by standard tomographic techniques. It is easiest to invert eq (18) using Fourier methods, as follows.

First define the one-dimensional Fourier transform of $f_t(v_s, \Omega)$ with respect to v_s as

$$\tilde{f}_t(k, \Omega)=\int dv_s f_t(v_s, \Omega)\exp(-ikv_s). \tag{19}$$

Inserting eq (18) into (19) and interchanging orders of integration, gives

$$\tilde{f}_t(k, \Omega)=\iint dx'dy'\sigma_0(x', y')$$

$$\cdot\exp[ik\Omega(x'\sin\Omega t-y'\cos\Omega t)]. \tag{20}$$

Now the two-dimensional Fourier transform, $\tilde{\sigma}_0(k_x, k_y)$, of $\sigma_0(x', y')$ is

$$\tilde{\sigma}_0(k_x, k_y)=\iint dx'dy'\sigma_0(x', y')$$

$$\cdot\exp[-i(k_xx'+k_yy')], \tag{21}$$

and, on comparing eqs (21) and (20), we have

$$\tilde{f}_t(k, \Omega)=\tilde{\sigma}_0(-k\Omega\sin\Omega t, k\Omega\cos\Omega t). \tag{22}$$

Equation (22) is the well-known central-slice theorem in tomography [4,5]. In the present context it states that $\tilde{f}_t(k, \Omega)$, evaluated at time t and spatial frequency k, is the two-dimensional spatial Fourier transform, $\tilde{\sigma}_0(k_x, k_y)$, of $\sigma_0(x', y')$ evaluated on a line in the (k_x, k_y) Fourier plane through the origin at angle Ωt with the k_x-axis. Thus, taking many revolutions of data and, during each revolution, stepping the value of v_s will generate sufficient data to provide complete coverage of the (k_x, k_y) Fourier plane, whereupon an inverse two-dimensional Fourier transform of $\tilde{\sigma}_0(k_x, k_y)$ yields the reconstruction $\sigma_0(x', y')$. Note that the required range of measured v_s values is from 0 to ΩR_{max}, where R_{max} is the largest radial dimension of the absorber.

One-Dimensional Imaging with Unknown v_a Distribution. In this case, let

$$\sigma_t(x, y, v_a)=\sigma_0(y, v_a)\delta(x).$$

For the one-dimensional absorber, again assume that the measurement is made as the absorber rotates past vertical at $t=0$. Then, substituting $\sigma_t(x, y, \gamma_a)$ into eq (15) and setting $t=0$, gives

$$f_0(v_s, \Omega)=\frac{1}{\Omega}\int dv_a\sigma_0[(v_s-v_a)/\Omega, v_a]. \tag{23}$$

We wish to solve for the two-dimensional function $\sigma_0(y, v_a)$, which has one spatial dimension (y) and one spectral dimension (v_a). Rewrite eq (23) as

$$f_0(v_s, \Omega)=\frac{1}{\Omega}\iint dy\,dv_a\sigma_0(y, v_a)\delta[y-(v_s-v_a)/\Omega].$$

Substituting into eq (19) and interchanging orders of integration, gives

$$\tilde{f}_0(k, \Omega)=\iint dy\,dv_a\sigma_0(y, v_a)\exp[-ik(\Omega y+v_a)]. \tag{24}$$

Now writing the two-dimensional Fourier transform of $\sigma_0(y, v_a)$,

$$\tilde{\sigma}_0(k_y, k_v)=\iint dy\,dv_a\sigma_0(y, v_a)$$

$$\cdot\exp[-i(k_y y+k_v v_a)],$$

and comparing to eq (24), we see that

$$\tilde{f}_0(k, \Omega)=\tilde{\sigma}_0(k\Omega, k).$$

This result resembles the central-slice theorem encountered earlier. Here $\tilde{f}_0(k, \Omega)$ is equal to the two-dimensional Fourier transform, $\tilde{\sigma}_0(k_y, k_v)$, of $\sigma_0(y, v_a)$ evaluated on a line in the (k_y, k_v) Fourier plane through the origin at angle $\tan^{-1}(\Omega)$ from the k_v-axis. Thus, by varying both k and Ω, complete two-dimensional coverage of $\tilde{\sigma}_0(k_y, k_v)$ in Fourier space can be achieved. The reconstruction of $\sigma_0(y, v_a)$ then follows on taking the inverse two-dimensional Fourier transform of $\tilde{\sigma}_0(k_y, k_v)$.

Two-Dimensional Imaging (Tomography) with Unknown v_a Distribution. Here we wish to reconstruct the three-dimensional function $\sigma_0(x', y', v_a)$. This is the most general inversion problem considered. Now rewrite eq (15) as

$$f_t(v_s, \Omega)=\frac{1}{\Omega}\iiint dx\,dy\,dv_a\sigma_t(x, y, v_a)$$

$$\cdot\delta[y-(v_s-v_a)/\Omega]$$

$$=\frac{1}{\Omega}\iiint dx'dy'dv_a\sigma_0(x', y', v_a)$$

$$\cdot\delta[-x'\sin\Omega t+y'\cos\Omega t-(v_s-v_a)/\Omega] \quad (25)$$

using eqs (10) and (12b) in the last step. Substituting eq (25) into eq (19) then gives

$$\tilde{f}_t(k, \Omega)=\iiint dx'dy'dv_a\sigma_0(x', y', v_a)$$

$$\cdot\exp[ik\Omega(x'\sin\Omega t-y'\cos\Omega t)-ikv_a]. \quad (26)$$

Writing the three-dimensional Fourier transform of $\sigma_0(x', y', v_a)$ as

$$\tilde{\sigma}_0(k_x, k_y, k_v)=\iiint dx'dy'dv_a\sigma_0(x', y', v_a)$$

$$\cdot\exp[-i(k_x x'+k_y y'+k_v v_a)],$$

and comparing to eq (26), we have

$$\tilde{f}_t(k, \Omega)=\tilde{\sigma}_0(-k\Omega\sin\Omega t, k\Omega\cos\Omega t, k).$$

This is the generalization of the central-slice theorem to three-dimensions. Thus, by suitably varying the three parameters v_s, Ω and t, full coverage in the three-dimensional Fourier space can be achieved, and an inverse Fourier transform of $\tilde{\sigma}_0(k_x, k_y, k_v)$ yields the reconstruction $\sigma_0(x', y', v_a)$.

4. Spatial Resolution and the Image Point Spread Function

In previous sections, we considered the idealized case of an infinitesimally narrow linewidth v_τ. This simplifies the mathematics, but implies that spatial resolution can be arbitrarily small. In this section, we show that spatial resolution is controlled by the natural linewidth v_τ; in particular, spatial resolution is proportional to the ratio of v_τ to the rotational velocity Ω of the absorber.

Below we derive the point spread function (PSF) of the two-dimensional tomographic reconstruction problem, with no v_a dependence for simplicity (the second case above). The PSF is by definition merely the reconstructed image of a two-dimensional Dirac delta function, or point object, and its width provides a reasonable measure of image resolution. Alternatively, the reconstructed image may be regarded as the true image convolved with the PSF.

To derive the point spread function in two dimensions, we repeat the above derivation using eq (14) in place of eq (15). Substituting

$$\sigma_t(x, y, v_a)=\sigma_t(x, y)\delta(v_a)$$

into eq (14) gives

$$f_t^{(\tau)}(v_s, \Omega)=\iint dx\,dy\,\sigma_t(x, y)P^{(\tau)}(\Omega y-v_s),$$

which is the first line of eq (18) with $\delta(\cdot)$ replaced by $P^{(\tau)}(\cdot)$. Now write this as

$$f_t^{(\tau)}(v_s, \Omega)=\iint dx'dy'\sigma_0(x', y')$$

$$\cdot P^{(\tau)}[\Omega(-x'\sin\Omega t+y'\cos\Omega t)-v_s]. \quad (27)$$

Writing the Fourier transform of $f_t^{(\tau)}(v_s, \Omega)$ with respect to v_s,

$$\tilde{f}_t^{(\tau)}(k, \Omega)=\int dv_s f_t^{(\tau)}(v_s, \Omega)\exp(-ikv_s), \quad (28)$$

substituting eq (27) into (28) and interchanging orders of integration, results in

$$\tilde{f}_t^{(\tau)}(k, \Omega)=\tilde{P}^{(\tau)}(k)\iint dx'dy'\sigma_0(x', y')$$

$$\cdot\exp[ik\Omega(x' \sin \Omega t - y' \cos \Omega t)]$$

$$=\tilde{P}^{(\tau)}(k)\tilde{\sigma}_0(-k\Omega \sin \Omega t, k\Omega \cos \Omega t), \quad (29)$$

where

$$\tilde{P}^{(\tau)}(k)=\int dv_s P^{(\tau)}(-v_s)\exp(-ikv_s) \quad (30)$$

is the Fourier transform of $P^{(\tau)}(-v_s)$. Equation (29) is merely eq (22) multiplied by $\tilde{P}^{(\tau)}(k)$.

We can evaluate $\tilde{P}^{(\tau)}(k)$ by inserting eq (7) into (30); integrating, the result is

$$\tilde{P}^{(\tau)}(k)=\exp(-kv_\tau).$$

Thus, the Fourier transform, $\tilde{\sigma}_0(k_x, k_y)$, of $\sigma_0(x', y')$ is weighted by the exponential radially-dependent function $\exp(-kv_\tau)$. The point spread function is obtained by setting $\tilde{\sigma}_0(k_x, k_y)=1$ in eq (29); as a result, the PSF is just the two-dimensional inverse Fourier transform of $\tilde{P}^{(\tau)}(k)$. Since $k\Omega$ is the radial coordinate in the Fourier plane, $\tilde{P}^{(\tau)}(k)$ has radial symmetry and the resulting PSF also has radial symmetry. Hence, the inverse two-dimensional Fourier transform of $\tilde{P}^{(\tau)}(k)$ can be evaluated in polar form:

$$\mathrm{PSF}(r')=\frac{\Omega^2}{2\pi}\int_0^\infty dk\, k\, \tilde{P}^{(\tau)}(k)J_0(\Omega k r')$$

$$=\frac{\Omega^2}{2\pi}\int_0^\infty dk\, k \exp(-kv_\tau)J_0(\Omega k r')$$

$$=\frac{v_\tau}{2\pi}\frac{1}{[(r')^2+(v_\tau/\Omega)^2]^{3/2}}, \quad (31)$$

where $J_0(\cdot)$ is the zero-order Bessel function and $r'=\sqrt{x'^2+y'^2}$. This is the desired point spread function whose width gives the image resolution. Let r_0' signify the full width at half maximum of eq (31); then

$$r_0'=0.76\, v_\tau/\Omega.$$

The important thing to note is that r_0' is inversely proportional to the rotational velocity Ω. Finally, one can show that PSF(r') becomes a two-dimensional Dirac delta function in the limit $v_\tau \to 0$, as required. As an example, for typical linewidths, v_τ, of less than a mm/s, this result shows that r_0' is on the order of a tenth of a millimeter when the absorber rotates at one revolution per second ($\Omega=2\pi$).

5. Imaging with an Extended Source (Non-Parallel Incidence)

In the latter two sections, we assumed parallel γ-ray incidence in the direction of the x-axis. Parallel incidence is easily achieved by placing the source far enough away so that it subtends a small angle at all points on the absorber. This is practical when the source is sufficiently strong to provide a γ-ray flux intercepting the absorber that results in an acceptable signal-to-noise ratio. Unfortunately, arbitrarily strong Mössbauer sources are not available, so that moving the source close to the absorber to maximize the incident flux may be important.

In the latter case, the source must be regarded as spatially extended, say, in the y-direction (fig. 4), and the incident γ-rays are no longer parallel. Assume that the extended source is moving in the x-direction at velocity v_s and that the absorber rotates with angular velocity Ω as before. Also, for simplicity, assume that the intrinsic velocity $v_a=0$. In this geometry, one can show that the component of velocity of a point on the rotating absorber and of a point on the source in the direction of the line joining them (i.e., along the line of flight of a γ-ray passing between the two points) are equal to each other (the resonance condition) if and only if the line defined by the two points passes through $(x=0, y=v_s/\Omega)$ in the stationary (x, y) coordinate system. To see this, refer to the line L in figure 5, which we suppose is the path of a γ-ray emitted from point A on the source. Suppose this path intersects the y-axis at height R, as shown. Then L is tangent to a circle around the axis of rotation of radius $R \cos \theta$, where θ is the angle between L and the x-axis. From previous arguments, all points in the absorber lying on L have the same component of velocity in the direction of L, namely $\Omega R \cos \theta$. But the additional component of velocity of the incident γ-ray along L due to the motion of the source is $v_s \cos \theta$, as can be seen from figure 5. The resonance condition is then obtained by equating the absorber and source components of velocity along L; thus setting $\Omega R \cos \theta = v_s \cos \theta$ results in

$R = v_s/\Omega$. Consequently, only those γ-rays moving along paths through $(x=0, y=v_s/\Omega)$ are resonantly absorbed.

The complete set of lines passing through this point and intercepting the source generates a sector, as shown in figure 4, where the boundaries of the sector are the two lines intersecting the end points of the extended source and coming together at the point $(0, v_s/\Omega)$ in the (x, y) system. The density of lines peaks at the point $(0, v_s/\Omega)$ and falls off in proportion to $1/|x|$ in the x-direction (fig. 6). Through the peak in the y-direction, the width of this function is much narrower; in particular, the width in the y-direction can be shown to be v_r/Ω, which is approximately the width of the point spread function derived previously for parallel incidence. Neglecting, for the moment, attenuation of the γ-rays through the absorber, the line-density function sketched in figure 6 may be equivalently interpreted as the probability density function of resonant absorption events per unit area, which is just proportional to the inverse of the sector area shown in figure 4.

The highly peaked distribution of the probability of resonance events is significant, since it implies that merely by varying v_s and counting absorption events as a function of time, it should be possible to generate a blurred image even without image reconstruction. Figure 4 shows that, by rotating the absorber, the γ-rays are effectively "focused" through the point $(0, v_s/\Omega)$. This focusing-like effect can be used to create a blurred image without further processing. A complete or deblurred image reconstruction cannot in this case be carried out analytically, but the reconstruction nevertheless can be performed using iterative algebraic reconstruction techniques (ART) [4,5]. The ART algorithms assume an initial estimate of the unknown image and then, on the basis of this estimate, recompute the measurements (line integrals of the resonant absorption coefficient). The recomputed measurements are then subtracted from the true measurements, giving rise to a set of error terms, which are then used to systematically adjust the current image estimate to reduce this error. When this iterative procedure is continued, it can be shown that the overall error tends to zero and, in the absence of measurement uncertainty and incomplete data, the reconstructed image converges to the true image. Such iterative approaches also make it relatively easy to incorporate attenuation effects in the algorithm.

In the above discussion, we assumed for simplicity that the extended source was one-dimensional (i.e., extended along the y-direction). If the source has some depth as well as height (i.e., some extension in the z-direction), the additional degree of freedom arising from variations in the x-component of the γ-ray velocity will broaden somewhat

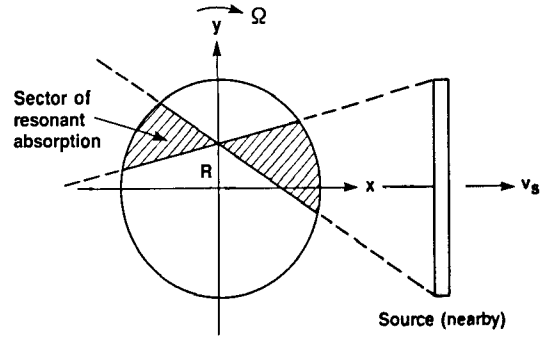

Figure 4–For an extended source (non-parallel γ-ray incidence), the line of sensitivity broadens into a sector of sensitivity bounded by lines subtending the source and intersecting at the point $(x=0, y=R)$, where $R\Omega = v_s - v_s$.

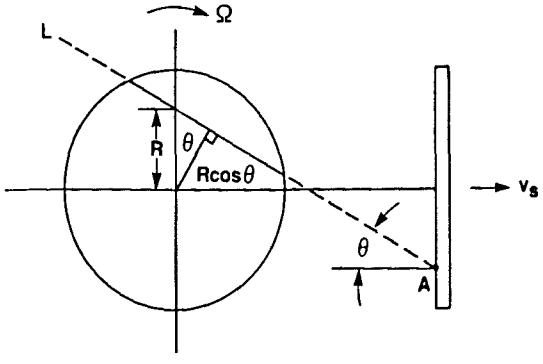

Figure 5–The line L signifies the path of a γ-ray emitted from one point on the extended source.

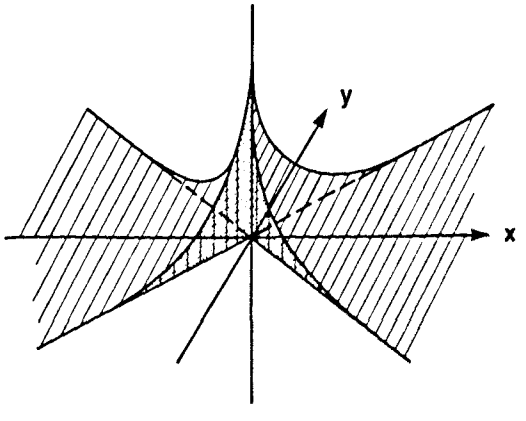

Figure 6–Probability distribution of resonant absorption per unit area over the sector of sensitivity in figure 4. The distribution falls off as $1/|x|$ along the x-axis and is approximately of width v_r/Ω along the y-axis.

the region of sensitivity beyond the sector illustrated in figure 4. To minimize this broadening effect, the source should be collimated in the z-direction as much as practical with a suitable arrangement of slits in this direction. A three-dimensional absorber could then be reconstructed on a "slice-by-slice" basis, as in two-dimensional x-ray tomography.

6. Applications

Applications of the technique to interior imaging appear to be limited to lighter materials, or absorbers of small size, that permit sufficient γ-ray penetration. One possibility is the imaging of composite materials, in which a Mössbauer element is embedded in a lighter matrix. Another possibility is surface imaging, whereby the surface of a flat absorber is rotated about an axis normal to the surface and a one-dimensional extended source is displaced a small amount from the plane of the surface. If all the impinging γ-rays have the same (or nearly the same) z-component of velocity, the region of sensitivity in which resonant absorption takes place will look much the same as the sector illustrated in figure 4. In this case, the value of v_s used previously should be replaced by the component of the source velocity in the plane of the surface.

Some potential high-resolution applications in materials science include the imaging of grain boundary segregation, the imaging of residual stress distributions, and the imaging of the distribution of magnetism in ferromagnetic materials due to perturbations in the Mössbauer spectra arising from variations in the magnetic hyperfine field.

7. Conclusion

In conventional Mössbauer spectroscopy, the measurement is spatially integrated over the absorber. For parallel γ-ray incidence, a rotating absorber generates a line of "sensitivity" over which resonant absorption takes place, where the location of the line is a function of the source velocity and the absorber rotational velocity. In particular, this line is parallel to the velocity of the source and passes through the point $(x=0,\ y=v_s/\Omega)$. For an extended source, the line broadens into a sector subtending the source and coming together at the point $(x=0,\ y=v_s/\Omega)$. For a highly extended source, the result is as if the γ-rays were effectively "focused" through the point $(x=0,\ y=v_s/\Omega)$. This focusing effect can be used to generate a blurred image of the absorption coefficient distribution in the absence of further processing when the measurements are recorded as a function of v_s and time (or the instantaneous absorber rotational position). Furthermore, by exploiting the three measurement degrees of freedom, v_s, Ω, and time (or rotational position), complete spectroscopic information can, in principle, be recovered as a function of position. Thus, Mössbauer spectroscopy can be performed in an imaging mode. Spatial resolution is proportional to the ratio of the natural linewidth v_τ to the rotational velocity Ω, but becomes rapidly signal-to-noise limited as the resolution increases.

References

[1] Danon, J., Lectures on the Mössbauer Effect, Gordon and Breach: New York (1968).

[2] Weisman, I. D.; L. J. Swartzendruber and L. H. Bennett, Nuclear resonances in metals: nuclear magnetic resonance and Mössbauer effect, in Techniques of Metals Research, R. F. Bunshah, ed., Vol. 6, Part 2, Wiley: New York (1973).

[3] Lauterbur, P. C., Image formation by induced local interactions: examples employing nuclear magnetic resonance, Nature **242** (March 16, 1973), 190–191; see also: J. L. Marx, NMR opens a new window on the body, Science **210** (Oct. 17, 1980), 302–305; P. Mansfield and P. G. Morris, NMR Imaging in Biomedicine, Academic Press: New York (1982).

[4] IEEE Trans. Nuclear Science **NS-21**, Special Issue on Image Reconstruction (June 1974).

[5] Comput. Biol. Med. **6**, Special Issue: Advances in Picture Reconstruction—Theory and Application (Oct. 1976).

Journal of Research of the National Bureau of Standards

International Intercomparisons of Photometric Base Units

Volume 92 Number 5 September-October 1987

Klaus D. Mielenz

National Bureau of Standards
Gaithersburg, MD 20899

In order to evaluate the worldwide consistency of practical implementations of the 1979 redefinition of the candela, the Consultative Committee for Photometry and Radiometry (CCPR) has conducted an international intercomparison of photometric base units. The intercomparison showed 0.8% agreement (one standard deviation) of independent luminous-intensity scale realizations by 15 national laboratories, and 0.6% agreement of luminous-flux scale realizations by 11 laboratories. The NBS candela and lumen agreed with the world mean within quoted uncertainty limits, and were shown to be consistent with one another within 0.5%.

Key words: candela; international; luminous flux; luminous intensity; photometry.

Accepted: July 23, 1987

In 1979 the 16th General Conference on Weights and Measures (CGPM) accepted a recommendation by the Consultative Committee for Photometry and Radiometry (CCPR) and redefined the SI unit of luminous intensity as follows:

> "The candela is the luminous intensity, in a given direction, of a source that emits monochromatic radiation of frequency 540×10^{12} hertz and has a radiant intensity in that direction of 1/683 watts per steradian."
>
> "The candela so defined is the base unit applicable to photopic quantities, scotopic quantities, and quantities to be defined in the mesopic domain."

This definition abrogated the platinum-point blackbody as the universal "primary standard of light" which defined the candela between 1948 and 1979. It established for the first time an exact numerical relationship between photometric and radiometric quantities. According to the current system of physical photometry that has been adopted by the International Commission on Illumination (CIE), this relationship is

$$Q_V = K_m \int d\lambda \, (dQ/d\lambda) \, V(\lambda) \, ,$$

where Q_V and Q are generalized luminous and radiant quantities, $V(\lambda)$ is the relative spectral luminous efficiency of the 1931 CIE standard observer, and K_m is the maximum spectral luminous efficacy which has been fixed as 683 lm/W by the new definition of the candela. The above expression holds for photopic light adaptation. Equivalent expressions, with K_m and $V(\lambda)$ replaced by appropriate other quantities as defined by the CIE, apply for scotopic and mesopic adaptation.

The main practical consequence of the 1979 candela definition and the CIE equations is that they allow choices of physical methods for realizing photometric scales. For example, lamps calibrated

About the Author: Klaus D. Mielenz is Chief of the Radiometric Physics Division in the Center for Radiation Research, which is part of the NBS National Measurement Laboratory.

as spectroradiometric standards can also be used as photometric standards once the above integral has been evaluated numerically. An alternative approach is the realization of photometric scales based on absolute detectors fitted with optical filters, so that the absolute spectral responsivity of the detector/filter combination represents the spectral luminous efficiency function $K_m V(\lambda)$.

The first of these approaches has been chosen by the National Bureau of Standards. Since 1979, NBS photometric standards have been derived from the NBS scale of spectral irradiance. The starting point of this derivation is the use of a gold-point blackbody to realize the 1968 International Practical Temperature Scale (IPTS-68), which is used in turn to measure the temperature of a variable temperature blackbody. The latter provides a scale of spectral radiance, which is then converted to a scale of spectral irradiance. All of the steps necessary to implement this measurement chain are performed on the NBS Facility for Automatic Spectroradiometric Calibrations (FASCAL). The NBS scale of spectral irradiance is maintained in a group of four 1000 W quartz halogen lamps. The primary calibration of the photometric working standards maintained at the Bureau is performed by making spectral irradiance measurements on FASCAL against these four quartz halogen lamps. The above integral is then evaluated using the adopted values of K_m and $V(\lambda)$ recommended by the CIE.

The detector approach to realizing the new candela has been adopted by several other national standardizing laboratories. Electrical substitution radiometers as well as absolute standard silicon photodiodes have been used in these scale realizations. Experimental photometric measurements based on absolute silicon photodiodes have been made at NBS in collaboration with the Hungarian Academy of Sciences and Office of Measures. These measurements have shown an over-all agreement at the 0.5% level with the above mentioned NBS photometric scale derived from blackbody based spectral irradiance measurements.

Following the redefinition of the candela, the CCPR allowed a period of three years for the realization of the new unit in different countries. In 1982, it organized an international intercomparison of luminous intensity and luminous flux measurements for two purposes. The first, scientific, purpose was to evaluate the world-wide consistency of diverse approaches to photometric scale realizations based on the new definition. The second purpose was to establish, for commercial reasons, the relationships between the photometric units maintained and disseminated by different national laboratories. The intercomparison, which took place during the 1984-86 period, was carried out under the following guidelines:

The participating national laboratories made absolute measurements based on independent scientific realizations of the new candela definition.

The International Bureau of Weights and Measures (BIPM) at Sevres, France, served as the convening laboratory. Since the BIPM did not have the facilities for independent scale realizations, it compared the scientific values reported by the participating laboratories to the values assigned to primary BIPM standard lamps based on means of previous intercomparisons.

Two types of gas-filled incandescent lamps (Osram Wi41G and NPL/GEC lamps) were selected for the luminous intensity measurements. Each national laboratory calibrated six lamps of either type, or four of each. The lamps chosen for the luminous flux intercomparison were gas-filled, high color temperature GEC lamps. Each laboratory measured six of these lamps. All lamps were operated at color temperatures of 2800 K$\pm$30 K, under constant current conditions, and with fixed polarity.

After a first round of measurements, the participating laboratories shipped their lamps to BIPM for comparison with the photometric standards maintained there. The BIPM then returned the lamps to the participants for repeat measurements.

The results of the intercomparison were presented at the 11th Session of the CCPR in October 1986. They are summarized in table 1.

Table 1. Results of the international intercomparison for the candela and lumen values.

	Candela	Lumen
Number of participating national laboratories:	15	11
Average quotient of BIPM value (cd or lm) to values obtained by participating laboratories:	0.990	1.007
Standard deviation of quotients:	0.77%	0.58%
Quotient of BIPM and NBS values:	0.985	0.997

The spread in the candela and lumen values reported by the different national laboratories was slightly better than in previous intercomparisons. Because of the wider range of techniques now used for realizing photometric scales, this was seen as giving confidence to the new definition of the photometric base unit. Accordingly, the CCPR recommended

> "that, by 1st July 1987, national laboratories make any necessary adjustment to the values attributed to their standards used for representing and disseminating the candela and the lumen in order to make them consistent with the definitions of these units,"
>
> "that, by the same date, these laboratories advise the BIPM of the magnitudes of the adjustments made and of their best estimates of the differences between their adjusted values and the mean values of the 1985 comparison."

Since NBS photometric scales have been based on the new candela definition since 1979, an adjustment of these scales was not necessary.

The intercomparison revealed a discrepancy in the photometric scales maintained at the BIPM. According to the average quotients shown on line 2 of table 1, the values attributed to the BIPM standards of luminous intensity were 1% lower than those corresponding to the mean candela of the intercomparison, and the values attributed to the BIPM standards of luminous flux were 0.7% greater than those corresponding to the mean lumen of the intercomparison. Since the BIPM units dated back to separate intercomparisons of luminous intensity and luminous flux measurements that were conducted in 1961 and 1952, the CCPR considered it mandatory to remove the 1.7% difference in the BIPM candela and lumen, and thus recommended

> "that the values attributed to the standards maintained by the BIPM as representing the candela and the lumen be adjusted, with effect from 1st January 1987, so as to conserve and disseminate the mean result of the 1985 comparison of realizations of the candela and the lumen."

The BIPM has since announced that this adjustment has been made.

With regard to the photometric scales maintained at NBS, it may be seen from table 1 that the ratios of the NBS luminous intensity and luminous flux values to the world mean of the intercomparison were $0.990/0.985=1.005$ and $1.007/0.997=1.010$. These differences fall well within the quoted uncertainties of 1.0% and 1.4%, respectively, for routine NBS luminous intensity and luminous flux calibrations. Nonetheless, research will be undertaken to investigate a possible deviation of the NBS lumen from the world mean. It should be noted, however, that the intercomparison showed the NBS candela and lumen to be consistent with each other to 0.5%.

Conferences / Events

FOURTH INTERNATIONAL CONGRESS ON OXYGEN RADICALS (4–ICOR)

More than 400 scientists and researchers from around the world at the Fourth International Congress on Oxygen Radicals in La Jolla, CA, last June considered the less benign effects of breathing oxygen.

Among the 200-plus papers presented at the 4-ICOR meeting organized by the NBS were those that: strengthened current theories on the importance of vitamins E and C in the diet, advocated the increase of fish and decrease of vegetable oil in the American diet, provided direct evidence of oxygen radical involvement in damage to organs that are resupplied with blood after being cut off from blood supply, and questioned the value of at least one high-tech health fad, hyperbaric (high-pressure) oxygen therapy.

Subtle biochemical mechanisms that may one day lead to prevention and new therapies to combat atherosclerosis, cancer, arthritis, various eye disorders, and an expanding list of other diseases, as well as the general effects of aging, were also discussed.

The last several years have seen an increasing awareness among chemists, biochemists, research physicians, and others of the key role played in biochemistry by "oxygen radicals," a variety of highly active chemical species derived from oxygen.

Although the idea of oxygen radicals has been around in one form or another since the 19th century, they have only been seriously considered in biochemistry since the 1960s, after researchers Joseph McCord and Irwin Fridovich of Duke University demonstrated the existence of a naturally occurring enzyme, superoxide dismutase (SOD) which seems to have no purpose other than to convert the simple oxygen radical to the more stable forms of hydrogen peroxide and molecular oxygen. The existence of SODs suggests that the superoxide radical, at least, is so prevalent in biochemical systems that enzymes have evolved to deal with it.

A related species, "singlet oxygen," was discovered in the early 1960s. Though not technically a radical, singlet oxygen spurred the study of the oxidation of organic and biomolecular systems. Radiation researchers contributed information on the extremely reactive hydroxyl radical to the growing list of oxygen species.

Since then, mushrooming research activity around the world has built up a picture of oxygen radicals intimately involved in a host of biochemical processes, both good and bad.

In brief, short-lived radicals are now believed to be a generally toxic by-product of cell processes, but with occasional benefits. One paper presented at this meeting by Kelvin J. A. Davies and Susan McKenna from the University of Southern California, for example, offers a new explanation of the mechanism by which "neutrophils" in the blood attack and destroy invading bacteria. According to this theory, the neutrophils initiate a rapid chain of reactions, beginning with the conversion of molecular oxygen to superoxide radicals and ending with the production of hypochlorous acid—common laundry bleach. This "bleach" then attacks the DNA and RNA synthesis mechanisms in the bacteria, destroying their ability to reproduce. This allows the neutrophils to dismantle it at leisure.

In general, the body seems to have a variety of natural mechanisms to keep oxygen radicals under control, transmuting them to other, less reactive forms and making use of them along the way. The system exists in a complex state of balance. Unfortunately, these mechanisms sometimes go awry, and it was the aim of the researchers gathered at 4-ICOR to understand how and why.

A growing study of evidence, much of it discussed at this meeting, implicates uncontrolled free radicals in a variety of diseases, including the two major killers in Western nations: atherosclerosis and cancer. Although still somewhat controversial, an increasing number of researchers believe that many of the basic effects of aging are due to the gradual accumulation of the products of reactions of oxygen radicals with cell components.

Some items raised at 4-ICOR include:

– Vitamins E and C are increasingly seen to be important in protecting cells from the harmful effects of oxygen radicals. Vitamin E, embedded in the cell's membranes, sacrifices itself to break an otherwise cell-lethal chain reaction initiated by oxygen radicals. Vitamin C, found in fluids outside the cell, sacrifices itself to repair the damaged vitamin E.

– The importance of regulating the *kinds* of fats in the diet is receiving increasing attention, according to University of Illinois researcher William Lands. By far the most common fats in the American diet are so-called "n-6 fatty acids," found in almost all vegetable oils, including corn, soybean, and safflower, and in the flesh of animals fed those grains. Although important to the body's mechanism of cell messenger molecules, says Lands, an excessive imbalance of these oils, and their biological products, has been implicated in a rogues' gallery of diseases ranging from headaches, menstrual cramps and hypertension through heart disease, stroke, coronary thrombosis, and cancer. Many of these effects apparently can be mitigated, according to Lands, by diminishing the use of n-6-type oils and increasing the intake of n-3-type oils found in green, leafy vegetables and, in particular, seafoods. "What's particularly impressive, I think," says Lands, "is that every single institute in the National Institutes of Health has requested researchers to explore this theory."

– Researchers working with Gregory Bulkley from Johns Hopkins University presented what may be the first direct evidence in a living system of the action of oxygen radicals in damaging organs that have been deprived of blood and then resupplied. This phenomenon, called "ischemia (blood deprivation) and reperfusion (resupply)" has received much attention recently because it seems to be one of the primary ways in which the brain, heart, and other organs are damaged after strokes, heart attacks, surgery, or other events that temporarily halt blood supply. Oxygen free radicals have been the chief suspects in the process, and the Johns Hopkins team reports the detection of the extremely low levels of light that are generated by free radical reactions, called chemiluminescence, in intact, living organs at reperfusion. Drugs that limit the action of the radicals in these cases may dramatically improve the chances of stroke victims to achieve full recovery.

– Hyperbaric oxygen chambers which involve breathing almost pure oxygen under pressure is seen by some researchers here as needlessly risky except in the treatment of certain conditions such as gas gangrene or stroke. Elevated levels of oxygen at high pressures bring on convulsions and death in lab animals, according to University of New South Wales researcher Dana Jamieson, with oxygen radical-mediated processes in the lung and brain vying to bring on death. "If you think of oxygen as a drug," observes Jamieson, "it has a very low therapeutic ratio. It would be difficult or impossible to get it by the FDA."

– Exactly how much exercise is good for you may be a more complicated question than generally realized, according to University of California researcher Lester Packer, who presented data to the congress showing that exercisers in training can develop temporarily decreased levels of vitamin E in their cells. Packer's group also presented the first preliminary evidence of a free-radical reductase, an enzyme which can repair vitamin E after it has been damaged by an oxygen radical.

The first International Congress on Oxygen Radicals was organized 10 years ago in Canada in an effort to bring together researchers from a wide variety of fields, including physical chemistry, physics, biomedicine, and medical research, to pool information on the behavior of oxygen radicals and their products. Subsequent congresses were held in Texas and West Germany.

One decision made at the current meeting was to form a new society—tentatively called "The Oxygen Society"—to encourage interdisciplinary research and discussion on the general topic of oxygen biochemistry. The society would complement the existing Society for Free Radical Research founded in Europe.

The Fourth International Congress on Oxygen Radicals, held June 28–July 3, 1987, was also sponsored by the National Heart, Lung, and Blood Institute; the International Life Sciences Institute; the National Cancer Institute; the American Industrial Health Council; and the Institute for Research on Aging. Seventeen major corporations and industrial associations also contributed to the congress.

Michael Baum
Public Information Division
National Bureau of Standards
Gaithersburg, MD 20899

Conferences / Events

CONFERENCE ON STANDARDS AND TRADE

The International Trade Administration and the National Bureau of Standards, of the Department of Commerce, sponsored a one-day Conference on Standards and Trade on May 5, 1987. The purpose of the Conference was to identify and explore possible actions by the Government and the private sector to enhance U.S. trade through promoting U.S. standards, and the technology they embody, in foreign countries and international organizations.

The Conference was co-chaired by the Honorable Bruce Smart, Under Secretary for International Trade, and Dr. Ernest Ambler, Director of the National Bureau of Standards. The first of three segments was comprised of presentations by officials of the U.S. Government: the Honorable Clarence Brown, Deputy Secretary of Commerce, the Honorable Michael Smith, Deputy U.S. Trade Representative, and Ambassador Diana Lady Dougan, U.S. Coordinator, Bureau of International Communications and Information Policy, U.S. Department of State. They stressed the need to improve the national trade picture, described ongoing efforts by the government under the GATT Agreement on Technical Barriers to Trade (the "Standards Code"), bilateral negotiations on standards-related trade problems, participation in treaty organizations and other government-to-government international committees, and the status of the current Uruguay Round of Multinational Trade Negotiations (MTN) talks. They expressed receptiveness to private sector views and their willingness to apply available resources to strengthen our trade position, especially in the international standards arena.

The second group of morning speakers addressed standards-related concerns of the business community. Dr. Peter Bell, Vice President of Corporate Technology, Norton Company, focused on export controls and expressed the desire for a single federal regulatory focus. Dr. Peter Bridenbaugh, Vice President for Research and Development, Alcoa, emphasized the need for U.S. leadership in technology and the development of the best technical standards possible. Mr. C. Scott Kulicke, Chairman and Chief Executive Officer, Kulicke and Soffa Industries, Inc., described the activities of the Semiconductor Equipment and Materials Institute (SEMI) and the necessity for rapid development of new standards in a changing technological environment, as well as participation by foreign nationals in standards-developing bodies, both in the United States and elsewhere.

Private sector participation in international standardization was the subject of the third part of the morning session. Dr. Robert Baboian, Chairman of the ASTM Board, echoed and underscored the importance of using the best technical standards available as *de facto* international standards, ASTM's role in international standards committee work, and in cooperating with the standards bodies of other countries. Dr. George S. Wham, Chairman, American National Standards Institute, described the private sector standards system and how ANSI functions as the member body to ISO and IEC.

Three Working Groups met in the early afternoon and submitted reports which may be summarized as follows:

Participation in International Standardization Activities, Chair: Catherine Kachurik, CBEMA staff and Director, X-3 Secretariat. The private sector should seek funding by collections under a budgeted, equitable system or by special assessment. Hosting meetings in the United States would reduce costs to U.S. participants and benefit foreign counterparts through favorable exchange rates.

The Group proposed media and educational campaigns to convince corporate executives and managers of the long-term value of participating in international standardization activities and to attract replacements for retiring "elder statesmen." The Government should seek industry opinion, be responsive and reactive to standards needs, and support positions in GATT talks and other negotiations.

Test Data Acceptance, Chair: Gerald Ritterbusch, Caterpillar, Inc. Initiatives to promote acceptance of test data by other countries should be pursued at all levels, including the current Uruguay Round of Multinational Trade Negotiations, bilateral negotiations, and the GATT Standards Code Committee. Voluntary laboratory accreditation programs, self-certification, third-party testing, and witnessed tests in the U.S. could reduce testing costs, with treatments matched to products and markets. An industry program should publicize certification programs, their costs, and significance.

Adoption of U.S. Standards, Chair: Barbara Boykin, Aerospace Industries Association. Industry must "think internationally" about standards and trade, abandoning nationalistic approaches and adapting to the needs of international markets; strengthen representation in ISO and IEC to encourage adoption of U.S. standards; pursue harmonization efforts with the European Community; promote awareness and availability of U.S. standards to potential users abroad; educate U.S. Government officials overseas about standards; preserve private sector leadership and enhance government-industry cooperation.

Texts of presentations, summaries of question-and-answer periods, and reports of the Working Groups will be published in Conference Proceedings, available from the NBS Office of Product Standards Policy in July.

Walter G. Leight
Office of Product Standards Policy
National Bureau of Standards
Gaithersburg, MD 20899